Technische Universität München
Fakultät für Physik

Master's Thesis for the Master of Science Degree
in
Applied and Engineering Physics

Quantitative Detection of Microscopic Lithium Distributions with Neutrons

Giulia Neri

Wednesday 10th August, 2016

Supervisor: Prof. S. Bishop
Second examiner: Prof. L. Oberauer

Abstract

The importance of the element lithium in the modern industrial society is continuously increasing. Lithium is used in many different fields, which are of key importance in the modern technology, such as rechargeable batteries, distributed energy storage and electromobility. Lithium is also widely used in glass and ceramics industries, as well as in alloys for aerospace technology.
Lithium has two stable isotopes, ^{7}Li and ^{6}Li, which have a natural abundance of 94.41% and 7.59% respectively [1]. One of the very special properties of ^{6}Li is its huge cross section for the absorption of low energetic neutrons ($\sigma_{n,th}$ = 940 barn) [2], which is one of the largest all over the nuclear chart.
The nuclear reaction $^{6}\mathrm{Li}\,(\mathrm{n},\alpha)\,^{3}\mathrm{H}$ represents the dominating decay channel after neutron capture.
In the framework of this thesis the spatially resolved detection of tritium particles from this reaction was used to reconstruct microscopic lithium distributions even in samples containing smallest amounts of this element. Samples were exposed to a flux of cold neutrons. Emitted charged particles were detected with a Position Sensitive Diode facing the target. Introducing a pinhole aperture between target and detector, the experimental setup worked like a "camera obscura", allowing to perform spatially resolved measurements. A reference target with a well-known homogeneous lithium surface density was used to calibrate the detector system, as well as a reference to determine the absolute lithium concentrations.
This method of spatially resolved detection of the ^{3}H particles from the $^{6}\mathrm{Li}\,(\mathrm{n},\alpha)\,^{3}\mathrm{H}$ reaction was introduced to two scientifically different fields. In the first case the lithium content in self-organized $\mathrm{TiO}_{(2-x)}$-C and $\mathrm{Si/TiO}_{(2-x)}$-C nanotubes electrochemically lithiated was reconstructed, for the first time in an absolute calibrated spatially resolved measurement. Titanium dioxide nanotubes are a candidate for a safe high density anode material in lithium-ion batteries.
Spatially resolved tritium detection was also used in the field of geology to reconstruct microscopic lithium distributions in geological samples of so called "pathfinder-minerals" containing lithium, like lepidolite ($\mathrm{K(Li,Al)_3(Si,Al)_4O_{10}(F,OH)_2}$) from a pegmatite.

Contents

Chapter 1

Introduction and Motivation

In recent years lithium demand and production increased significantly, mostly driven by its application in lithium-ion batteries, which are considered to be one of the most promising rechargeable energy storage systems. Lithium-ion batteries are already widely used in electric and hybrid automobiles, as well as in electronic mobile devices such as laptops, cell phones and cameras. In 2013 consumers bought a remarkably high number of lithium-ion cells, 5 billions of units, to supply mobile devices and electric vehicles [3], corresponding to approximately one cell per person per year.
As reported by the U.S. Geological Survey, the global production of lithium increased by about 6% in 2014 [4], followed by a slight growth in 2015 [5]. Batteries, together with ceramics and glass, are estimated to be the two largest lithium markets globally, accounting for 35% and 32% respectively [5].
Salt lakes brine containing lithium chloride as well as granitic pegmatites represent the two most relevant sources of lithium. In the late 1990s lithium was extracted for the most part from subsurface brines, due to the lower costs of production. However, in recent years the extraction of lithium from mineral deposits regained relevance, driven by the increasing lithium demand, and it is estimated that about one half of the worldwide lithium supply in 2015 came from mineral sources [5]. As the growth in lithium demand is not expected to stop in the next years and the number of economically accessible lithium mines is still rather low, it is getting more important to search for new lithium deposits - as well as exploit the already existing ones in a sustainable way.
Geochemical processes leading to the formation of lithium aggregations in the earth crust are not completely understood. Studying the distribution of lithium aggregations in the different crystallites of lithium-enriched minerals and investigating how they grow into the mineral, will help getting a better understanding of these processes. Therefore, in the framework of a scientific geological basic research, the so-called "pathfinder-minerals" containing lithium - such as spodumene ($LiAlSi_2O_6$), lepidolite ($K(Li,Al)_3(Si,Al)_4O_{10}(F,OH)_2$), petalite ($LiAlSi_4O_{10}$), lithiophilite ($LiMnPO_4$) and hectorite ($Na_{0.3}(Mg,Li)_3(Si_4O_{10})(F,OH)_2$)) [6] - are currently studied.
In the framework of this thesis a new precision method - based on the spatially

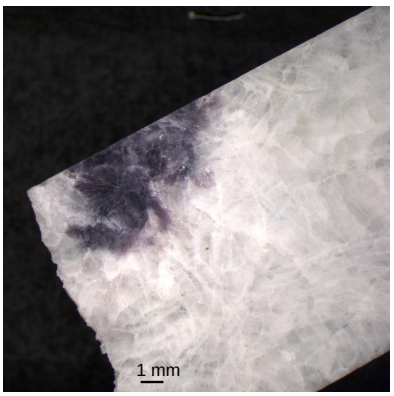

Figure 1.1: Photo of a pegmatite sample from Western Australia. The white-coloured region of the sample consists of feldspars, whereas the purple-coloured region contains lepidolites.

resolved detection of tritium particles from the neutron capture reaction by ^{6}Li - was successfully applied to reconstruct the local lithium content in such "pathfinder-minerals" containing lithium, like lepidolite from a pegmatite (see Fig. 1.1). This project was developed in collaboration with the Helmholtz Zentrum Dresden Rossendorf and the Helmholtz-Institut Freiberg für Ressourcentechnologie.

The use of lithium in rechargeable battery cells for electromobility is currently limited by two important issues. The power density is probably the most important for long distance rides. Fossil fuels still overcome even the best rechargeables by more than one order of magnitude. But also charging speed represents a central aspect. Both issues could be overcome by the developement of new electrode materials.
The Material- and Nanochemistry Group[1] led by Prof. Julia Kunze-Liebhäuser at the Institute of Physical Chemistry in Innsbruck is developing a fundamentally new type of such electrode materials based on nanotechnology. In particular they are currently studying titanium dioxide nanotubes, which represent a very promising candidate for a safe high density anode material in lithium-ion batteries.
Nanostructured titanium dioxide offers several advantages, such as a fast recharging speed due to the large surface of the nanotubes, as well as high lithium densities. Moreover titanium dioxide has a safe lithiation potential between 1.2 V and 2.0 V *vs.* Li [7], a low molar mass, a very high natural abundance and it is non-toxic.
The Innsbruck group is also developing a special technique to coat the nanotubes with a thin film of silicon of about 10 nm (see Fig. 1.2), which significantly increases the performance of the lithium cell with respect to non-coated nanotubes [8].

[1] `https://www.uibk.ac.at/physchem/materials-nanochemistry/welcome/`

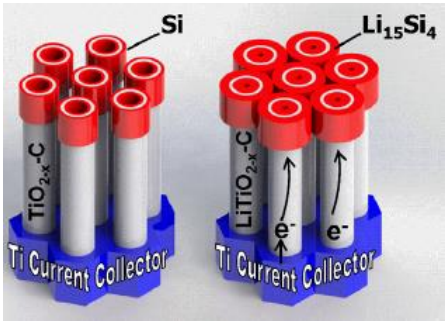

Figure 1.2: Self-organized Si/TiO2-x-C nanotubes charged with lithium ions. Source: [8].

Performing very precise measurements of lithium storage capacities has a central role by investigating nanostructured anode materials.
In the framework of this thesis the spatially resolved detection of tritium particles was successfully applied to reconstruct the local lithium content in self-organized $TiO_{2\text{-}x}$-C and Si/$TiO_{2\text{-}x}$-C nanotubes electrochemically lithiated for the first time. The project was developed in collaboration with the Innsbruck group. With this new precision method, even smallest amounts of lithium intercalated into the self-organized titanium dioxide nanotubes were detected, without removing lithium from the electrodes. But the very special advantage of the lithium detection with neutrons consists of the possibility to perform spatially resolved measurements, allowing to resolve any inhomogeneity in the lithium surface density over the electrode area. Results obtained from the spatially resolved detection of tritium particles were compared with those obtained from the electrochemistry - measuring the electrochemical charge upon lithiation/delithiation - for the same electrodes.

Chapter 2

Measurement Method

The detection method presented here is based on the $^6\mathrm{Li}\,(\mathrm{n},\alpha)\,^3\mathrm{H}$ reaction with a cross section of $\sigma_{n,th} = 940$ barn for thermal neutrons [2]. It is used to measure the local lithium concentration even in samples containing smallest amounts of this element. In this chapter the physical properties of ^{6}Li will be briefly presented and the measurement method developed for the detection of microscopic lithium distributions will be described. In particular the chapter will focus on modifications carried out in the framework of this thesis to optimize an existing detector setup, in order to determine the local lithium concentration in thicker samples.

2.1 Properties of ^{6}Li

With atomic number $Z = 3$ lithium is the third element in the periodic table of elements, after hydrogen and helium. In its pure form lithium is a soft, silver metal belonging to the group of alkali metals. Lithium has an atomic weight of $M = (6.941 \pm 0.002)$ u [2] and it is the lightest metal with a density of $\rho = 0.534\ \frac{\mathrm{g}}{\mathrm{cm}^3}$ at room temperature [9].
The name "lithium" comes from the greek "lithos", which means "stone". It was first detected in 1817 by Johan August Arfwedson, as he was analyzing petalite ore. Pure lithium was first isolated from its salts in 1821 by William Thomas Brande and in 1855 larger quantities of this pure metal were produced by Robert Bunsen and Augustus Matthiessen through electrolysis of lithium chloride [9].
Lithium naturally occurs in two stable isotopes, ^{6}Li and ^{7}Li, having a natural abundance of $(NA)_{^6Li} = (7.59 \pm 0.04)\,\%$ and $(NA)_{^6Li} = (92.41 \pm 0.04)\,\%$ respectively [1]. One of the most peculiar properties of ^{6}Li is its high neutron capture cross section of $\sigma_{n,th} = (940 \pm 4)$ barn [2] for thermal neutrons ($E_{n,th} = 25$ meV). The lithium measurements performed as part of this thesis have been carried out at the PGAA[1] facility of the FRM[2] (see Chapter 3.2), where cold neutrons with an average energy of $E_n = 1.83$ meV are used. For neutrons with this energy the neutron absorption

[1] http://www.mlz-garching.de/pgaa
[2] https://www.frm2.tum.de/en/home/

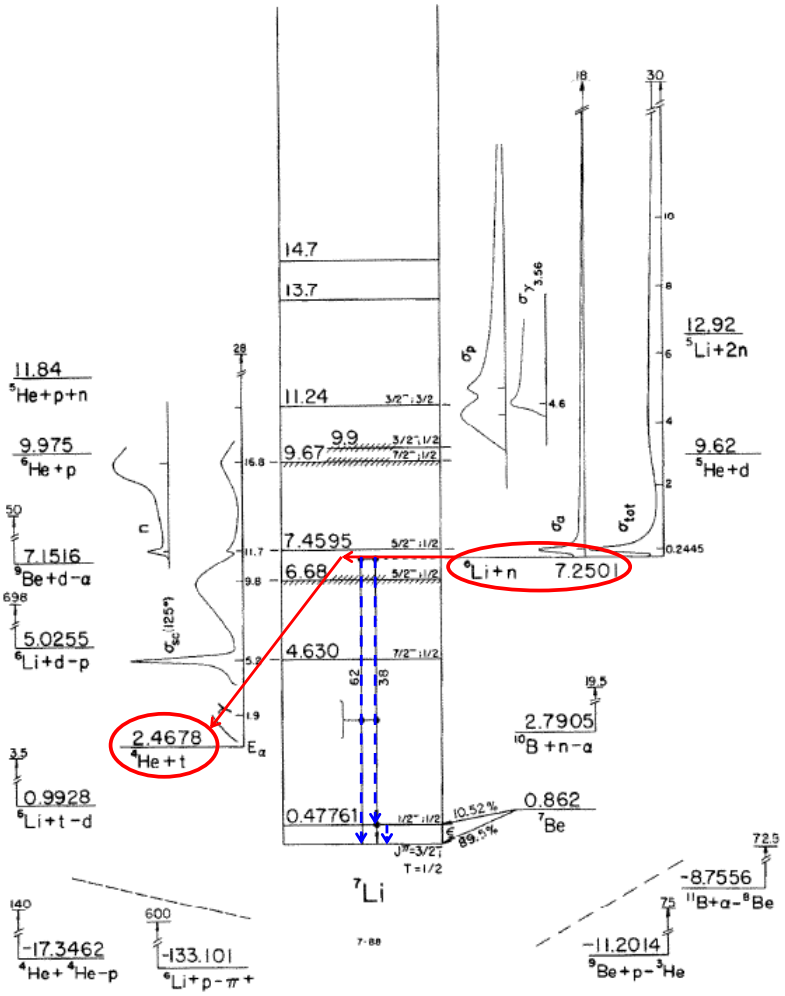

Figure 2.1: Energy levels of ^{7}Li. Energy values in MeV are related to the zero energy ground state. Energy levels or transitions which are uncertain are marked with dashed lines; levels which are particularly broad are cross-hatched. Total angular momentum J, parity, and isospin T are written on the levels. The neutron capture reaction of ^{6}Li is pointed out in red. Original picture from: [10].

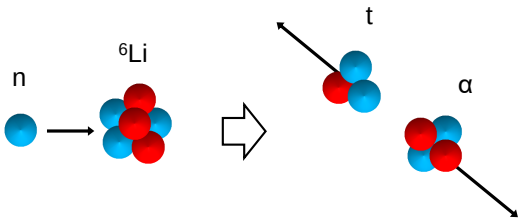

Figure 2.2: Schematic representation of the $^6\mathrm{Li}\,(\mathrm{n},\alpha)\,^3\mathrm{He}$ nuclear reaction. Blue particles represent neutrons, whereas red particles are protons.

cross section of ^{6}Li is even higher and amounts to $\sigma_n\,(E = 1.83\ \mathrm{meV}) = 3474$ barn, according to the following scaling formula:

$$\frac{\sigma_n}{\sigma_{n,th}} = \sqrt{\frac{E_{n,th}}{E_n}} \tag{2.1}$$

When a ^{6}Li nucleus captures a neutron, the resulting compound nucleus, ^{7}Li, is typically in a highly excited state. The de-excitation process of $^7\mathrm{Li}^*$ can occur over several possible reaction channels, which are illustrated in Fig. 2.1.
In the center of Fig. 2.1 the energy level scheme of ^{7}Li [11] is plottet. The energy values in MeV are related to the ground state. On the right, the neutron capture reaction of ^{6}Li is pointed out in red. The excitation energy of ^{7}Li after the absorption process amounts to $E_{free} = 7250$ keV. It corresponds to the difference between the binding energies of ^{6}Li and ^{7}Li [1]:

$$A_{^6\mathrm{Li}} \cdot \left(\frac{BE}{A}\right)_{^6\mathrm{Li}} - A_{^7\mathrm{Li}} \cdot \left(\frac{BE}{A}\right)_{^7\mathrm{Li}} = 6 \cdot 5332\ \mathrm{keV} - 7 \cdot 5606\ \mathrm{keV} = -7250\ \mathrm{keV} \tag{2.2}$$

A corresponds to the number of nucleons and $\frac{BE}{A}$ to the binding energy per nucleon. As already mentioned above, directly after the neutron capture $^7\mathrm{Li}^*$ is typically in a highly excited state.
The dominating exit channel is the emission of an alpha (^4He) and a tritium (^3H) particle, represented by the red arrows in Fig. 2.1. Assuming to deal with thermal or cold neutrons, whose kinetik energy can be neglected, and assuming ^{6}Li nuclei at rest, alphas and tritons are emitted in opposite direction at an angle of $\Theta = 180°$, which is a direct consequence of momentum conservation (see Fig. 2.2). The amount of energy released by this reaction (Q-value) is equal to $Q = 4782$ keV [10] and is distributed among the two daughter nuclides the alpha and the tritium as kinetik energy, according to energy and momentum conservation. Alphas are emitted with

a fixed energy of $E_\alpha = 2055$ keV and tritons with an energy of $E_t = 2727$ keV.
The excited ^{7}Li* can also promptly decay into the ground state by emitting gamma-rays at specific energies. The $^6\mathrm{Li}\,(n,\gamma)\,^7\mathrm{Li}$ reaction channel is represented in Fig. 2.1 by the blue dotted lines. Here ^{7}Li can directly go down to the ground state emitting a gamma ray with an energy $E_\gamma = (7245.91 \pm 0.04)$ keV [2], or first decay into the first excited state also by and then into the ground state by emitting gamma rays of energies $E_\gamma = (6768.81 \pm 0.04)$ keV and $E_\gamma = (477.595 \pm 0.03)$ keV [2] respectively. The cross section for a $^6\mathrm{Li}\,(n,\gamma)\,^7\mathrm{Li}$ reaction, which amounts to $\sigma_\gamma = (39 \pm 3)$ mbarn [2], is rather low compared to the total neutron capture cross section of ^{6}Li, which makes the de-excitation of ^{7}Li by gamma rays emission very unlikely.

2.2 Experimental Concept

For the quantitative position sensitive measurement of smallest lithium concentrations a special detector setup was designed and constructed in the framework of a DFG Project (GE 2296/1-1) and the PhD thesis of Josef Lichtinger [12] at the TUM[3].
Samples containing lithium are placed between two position sensitive silicon detectors and exposed to a flux of cold neutrons (see Fig. 2.3). ^{6}Li isotopes absorbing a neutron decay into a tritium and an alpha particle, which are emitted in opposite direction as described before ($E_t = 2727$ keV and $E_\alpha = 2055$ keV). Due to the large energy deposit of those particles in the thin silicon detectors there is already a rather good separation from the typical background in this kind of experiment i.e. γ and β particles.
If the measured sample is thin enough to let alphas and tritons escape on both sides of the sample, a coincident detection of both particles is possible. This not only allows to get information about the integral lithium content in the target and a much more powerful background suppression, but also permits to reconstruct the emission position of the mother nuclides, thus creating a "map" of the local lithium concentration in the sample.
Using position sensitive silicon detectors (PSD) the impact position of particles hitting the detectors is measured. Two events which are detected in a coincidence window of $\Delta t < 200$ ns in both detectors and having an energy of 2733 keV and 2055 keV respectively originate typically from the same ^{6}Li atom. Connecting the impact position of both events and intersecting that line with the target plane, it is possible to reconstruct the position in the sample where the reaction of a ^{6}Li isotope

[3] Technische Universität München, `https://www.ph.tum.de/`.

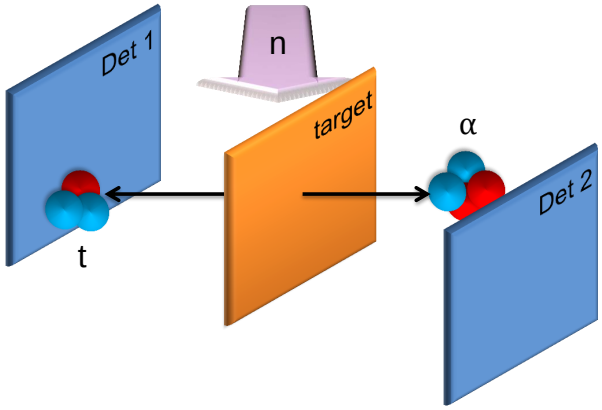

Figure 2.3: Schematic representation of the experimental setup for the lithium measurement in very thin samples. The sample is placed between two PSDs and exposed to a flux of cold neutrons, which gives rise to the nuclear reaction $^6\mathrm{Li}\,(n,\alpha)\,t$. Tritium and alpha particles are emitted in opposite direction. The coincident detection of both particles gives information about the position dependent lithium content.

and a neutron took place, as it is shown in Fig. 2.3.

The above described experimental setup has already been developed for the measurement of very thin samples, in particular for the study of organic tissue [13]. This development was a major part of the PhD thesis of Josef Lichtinger, which is recommended for a more detailed description [12]. The maximum sample thickness for which a coincident particle measurement was developed amounts to about $\mathrm{d} < 1\frac{\mathrm{mg}}{\mathrm{cm}^2}$ for typical organic composit material formed out of light nuclei.
Purpose of this thesis is to determine the local lithium concentration in thicker samples. At this scope the previously described setup has been modified for the lithium measurement in thicker targets. A schematic representation of the modified experimental setup is shown in Fig. 2.4. The neutron flux again hits the front side of the target at an angle of 25°. Only particles emitted in the +x direction can escape from the target and hit the detector. Particles which propagate in the opposite direction deposit their whole energy in the sample material being stopped there. Therefore a coincident measurement can not be performed and only one detector is used.
To perform a position dependent lithium measurement a pinhole aperture is placed in front of the target (see Fig. 2.2). It consists of a foil of Polytetrafluoroethylene (PTFE), thick enough to stop tritons and alphas, with a small hole in the center. Tritium and alpha particles pass through the small hole and project an inverted

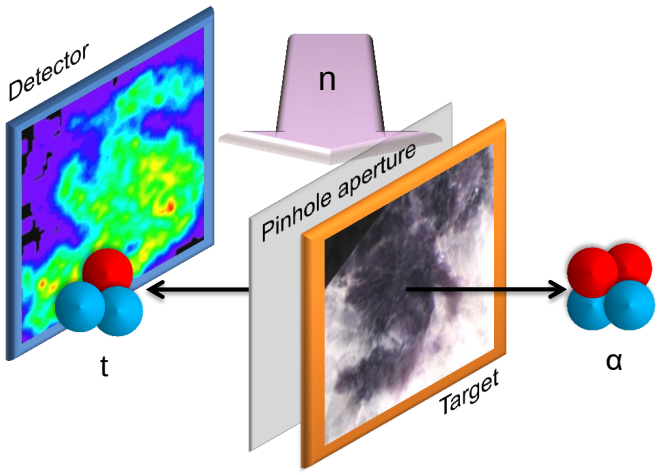

Figure 2.4: Schematic representation of the modified experimental setup for the lithium measurement in thicker samples. Under neutron exposure ^{6}Li isotopes decay emitting a tritium and an alpha particle in opposite direction. Particles emitted in the +x direction can leave the target and are detected with a PSD detector, whereas particles propagating in the opposite direction are stopped in the sample material. To map the lithium distribution in the sample onto the detector a pinhole aperture is placed between the target and the detector.

"image" of their origins onto the detector plane. In that way a map of the lithium distribution in the sample is created onto the detector, as it is shown in Fig. 2.4.
The concept of the pinhole aperture imaging arises from the camera obscura.
The camera obscura is a dark box with a small hole permitting the light to enter. If a white screen is placed opposite to the hole, the external scenario will be projected inverted onto the screen.
The technical principles of the camera obscura have been known since antiquity. The first to write about that concept was Aristotle in the fourth century B.C. in his *Problemata physica*; he probably used this mechanism to observe a solar eclipse. The broad use of the camera obscura in art, theatre and architecture started in the Renaissance - the first scientific study of the camera obscura goes back to Leonardo da Vinci - assuming later a central role in the history of photography.
Introducing the pinhole aperture in front of the target, the one-detector setup works like a camera obscura, allowing to reconstruct the spatially resolved lithium concentration in the sample.
Using the pinhole aperture the lithium pattern is not only projected onto the detector upside down, but also enlarged. The magnification factor is given by the ratio

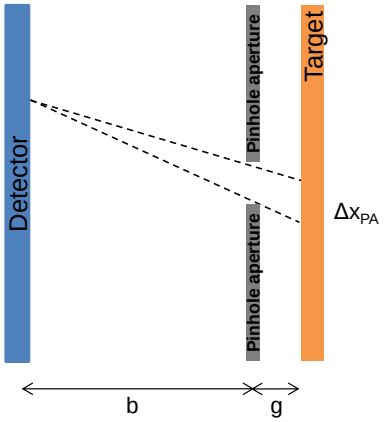

Figure 2.5: Schematic representation of the pinhole aperture imaging. The concept arises from the camera obscura. The finite size of the pinhole aperture influences the spatial resolution of the measurement.

$\frac{b}{g}$ of the image distance b and the object distance g (see Fig. 2.2). Varying the two parameters b and g it is possible to adjust the size of the target area which is projected onto the detector and therefore which can be analyzed.
The finite size of the pinhole aperture D influences the spatial resolution of the measurement σ. This is given by a contribution from the detector itself, as well as from a contribution due to the presence of the pinhole aperture, which are summed up as $\sigma^2 = \sigma_{xy}^2 + \sigma_{PA}^2$. The influence of the pinhole aperture is approximated as $\frac{D}{\sqrt{12}}$, where D is the diameter of the aperture. The intrinsic resolution of the detector σ_i was measured to $\sigma_i = 0.2$ mm at E = 2 MeV in each dimension x and y [12]. This is relevant only in case of a small aperture.
Information about the total lithium content in the target can still be extrapolated from the total number of tritons or alphas hitting the single detector. To avoid large systematic uncertainties a reference target with a well-known lithium concentration is used. Replacing the target by the reference target the geometric acceptance as well as the detection efficiency are calibrated. This procedure is described in Chapter 4 in more detail.

Chapter 3

Experimental Setup

The experiment performed as part of this thesis was carried out at the PGAA[1] facility at the research neutron source FRMII[2]. A brief introduction about the FRMII and the PGAA facility will be given in this chapter. Characteristics and structure of the PGAA instrument will be presented. In particular the chapter will focus on the description of the detector-target system developed for the lithium measurements and inserted in the PGAA vacuum chamber. Detector, target chamber, target holder, system of collimators, as well as the measurement procedure are described in detail.

3.1 Forschungs-Neutronenquelle Heinz-Maier-Leibnitz (FRM II)

The research neutron source Heinz-Maier-Leibnitz (FRM II) in Garching came into operation for users in 2005 and represents one of the most advanced neutron sources worldwide. About 1000 scientific experiments are carried out every year at the FRM II and about 4000 visitors annually come to Garching from all over the world to visit the research reactor[3].
The FRM II generally operates in cycles of 60 days, followed by maintenance breaks. During the operation phases a lot of different experiments and projects are carried out in parallel, dealing with a wide variety of scientific, technical or medical topics. They range from basic research, such as the study of fundamental properties of neutrons, to technically oriented applications, such as the homogeneous doping of silicon for the semiconductor industry, the study of materials, the production of radioisotopes for medicine and industry or the theraphy of malignant tumors [14].
The FRM II is a highly-efficient research neutron source. With respect to its thermal power of 20 MW FRM II is able to produce a neutron flux of $\Theta_{\mathrm{n,th}} \leq 8 \cdot 10^{14}\ \frac{\mathrm{n}}{\mathrm{cm^2 \cdot s}}$ [3].

[1] http://www.mlz-garching.de/pgaa
[2] https://www.frm2.tum.de/en/home/
[3] https://www.frm2.tum.de/en/about-us/facts-figures/

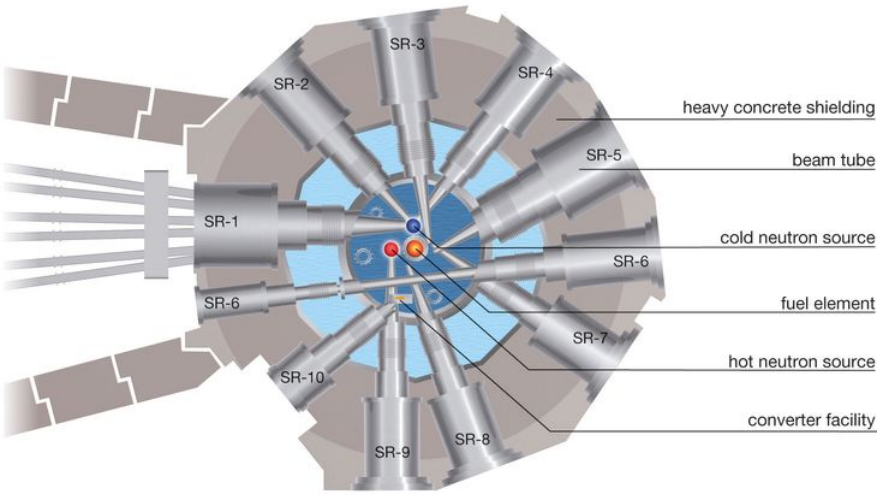

Figure 3.1: Section of the reactor pool with the eleven beam tubes providing neutrons for the different experiments. Beam pipes number 3, 5, 7 and 8 provides thermal neutrons; they point exactly at the peak of the thermal neutron flux distribution in the moderator tank. Beam tubes 1, 2 and 4 point at the moderator tank where cold neutrons are produced and serve up to 32 instruments with cold neutrons. Picture from source [4].

Neutrons used at FRM II are not monoenergetic, but cover a wide range of energies. The fission of uranium first provides fast neutrons with high energies in the MeV range. However, about 40% of all experiments as well as the nuclear chain reaction in the reactor core itself need thermal neutrons (3-150 meV). The energy of fast neutrons is therefore reduced through collisions with heavy water molecules in the moderator tank (see Fig. 3.3).
Secondary sources are used to further shift the peak of the neutron flux distribution to higher or lower energies, producing *hot*, *cold* and in the future also *ultra cold* neutrons, each of which having specific applications. For the different neutron sources see Fig. 3.3.
The hot source is a graphite block of 14 kg, which heats up thermal neutrons to $40 - 10^3$ meV, whereas the cold source consists of an additional cold moderator tank where the energy of neutrons is reduced to 5 meV or less (see Fig. 3.3). The tank is filled with 16 l of liquid deuterium at a temperature of T = 25 K.

[4] `https://www.frm2.tum.de/en/the-neutron-source/reactor/guiding-the-beams/`

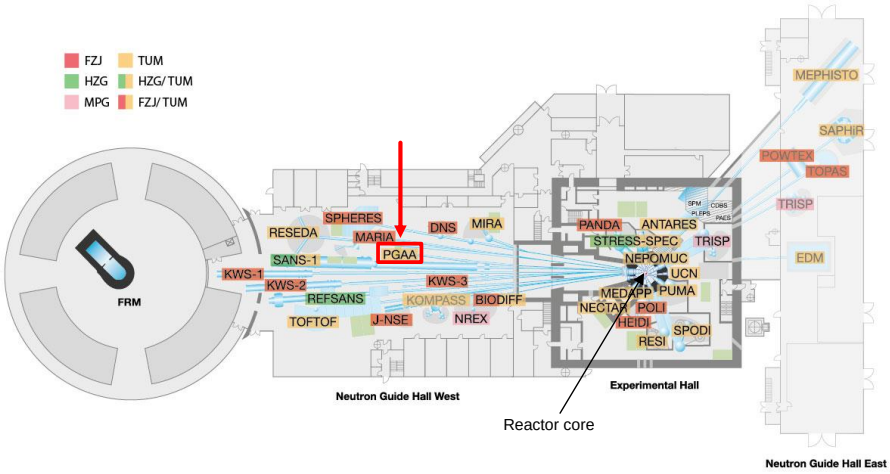

Figure 3.2: Schematic representation of the measurement facilities at Heinz-Maier-Leibnitz Zentrum (MLZ), according to partners (FZJ - Forschungszentrum Jülich, TUM - Technische Universität München, HZG - Helmholtz-Zentrum Geesthacht, MPG - Max Planck Society). Highlighted in red the PGAA facility, where the lithium measurements have been performed. Original picture from: [5].

In particular cold neutrons are relevant for this thesis since thay are used at the PGAA facility, where the lithium measurements have been performed.

3.2 PGAA Facility

One of the instruments at FRM II using cold neutrons is the Prompt Gamma-ray Activation Analysis (PGAA) [15] facility.
PGAA uses the neutron capture reaction to study the elemental composition of solid, liquid and gaseous samples without damaging them. It is also possible to get information about the concentration of the different elements. Typically concentrations down to the ppm range can be detected.
A neutron capture reaction occurs when the wave functions of a sample nucleus and a neutron overlap forming a heavier nucleus: ${}^{A}Z + n \rightarrow {}^{A+1}Z + \gamma$. The compound nucleus is typically in a highly excited state and promptly decays into the ground

[5] http://www.mlz-garching.de/instruments

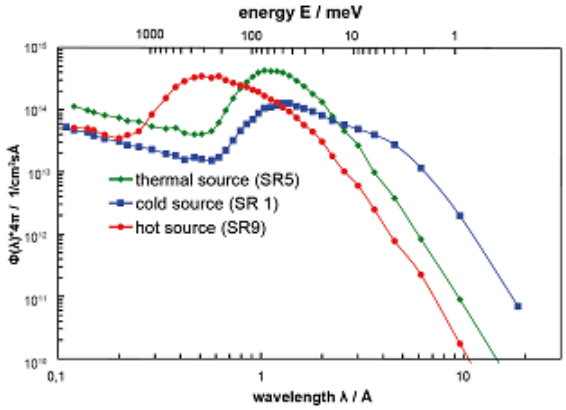

Figure 3.3: Neutron flux spectrum of the three different sources operated at 20 MW reactor power at the FRMII. Source: [16].

state by emitting gamma-rays at specific energies (prompt gamma activation).

Samples are activated inside the PGAA sample chamber (Fig. 3.4). They are fixed in a vertical sample holder with six positions. From the PGAA control station a batch run for all six samples can be started. The measurement is performed automated with help of a motor which drives the sample holder vertically along the target chamber. Emitted photons are revealed with Compton-suppressed high purity germanium detectors. Energies ranging from about 80 keV to 10 MeV can typically be detected. From the analysis of the recorded energy spectra, the well known efficiency curve of the detector and the transition probabilities from different nuclear states, the elemental composition of the sample is reconstructed.

As already mentioned above cold neutrons are used at PGAA. A neutron guide brings them from the cold source in the moderator tank to the instrument. The average energy of the neutrons amounts to 1.83 meV, corresponding to a wavelength of 6.7 Å [6].
The end part of the neutron guide has special neutron mirrors which elliptically focus the beam, providing a very well focused beam and an extremely high cold neutron flux at the target position in the sample chamber. The last 6.9 m of the neutron guide are divided into two parts, a fixed one (with a length of about 5.8 m) and a removable one (with a length of about 1.1 m, called *elliptical nose*) [17]. Each setup configuration - with or without the elliptical nose - defines specific measurement conditions.
All lithium measurements have been performed using the elliptical nose. This

[6] `http://www.mlz-garching.de/pgaa`

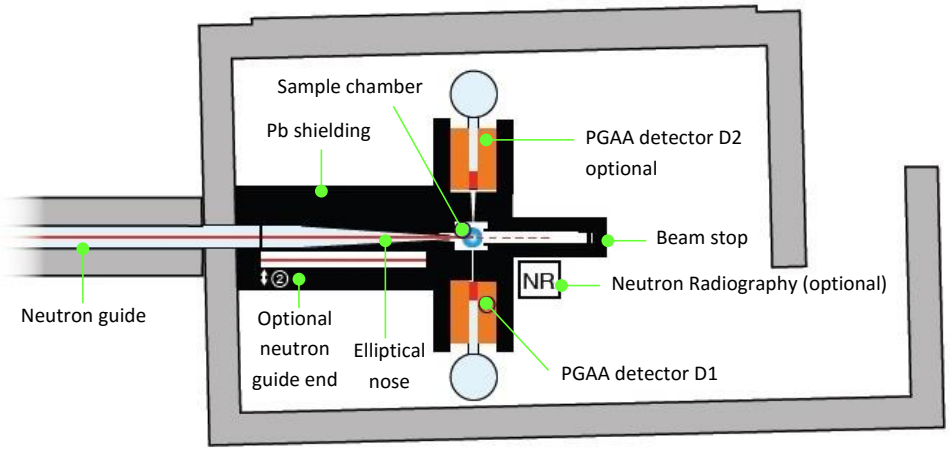

Figure 3.4: Schematic representation of the PGAA cave at the FRM II. A neutron guide brings cold neutrons from the cold source to the instrument. In the last 6.9 m of the neutron guide mirrors elliptically focus the beam, providing a very well focused and extremely high neutron flux at the measuring position. A l = 1.1 m long elliptical nose sight in front of the target chamber can be replaced by a regular neutron guide not used in this experiment. In normal PGAA operation samples are activated inside the PGAA sample chamber and gamma-rays are detected with a Compton-suppressed spectrometer. Original picture from: [16].

provides a neutron beam of minimum dimensions (about 11×16 mm^2) and a higher maximal thermal equivalent neutron flux, which amounts to $\Theta_{\mathrm{n,th}} \leq 5 \cdot 10^{10}$ $\frac{\mathrm{n}}{\mathrm{cm}^2 \cdot \mathrm{s}}$ [7]. The measurement conditions established for the lithium measurements are summerized in table 3.1.

3.3 Instrument Extensions for the Lithium Measurement

To perform the lithium measurements a specific detector setup (see also [12]) was developed, implemented and used.
It consists of one or two position sensitive silicon detectors, a small additional in-chamber collimator, an additional collimator outside the chamber and several PTFE (best known as Teflon[8]) components to shield the detectors from background particles (see Fig. 3.6). This detector setup is placed into the PGAA sample chamber.

[7] http://www.mlz-garching.de/pgaa
[8] Teflon™

Measuring conditions	
Elliptical nose	✓
Beam size	11×16 mm^2
Max. thermal equivalent neutron flux	$5 \cdot 10^{10}$ $\frac{\text{n}}{\text{cm}^2 \cdot \text{s}}$
Average neutron energy	$\text{E}_n = 1.83$ meV
Pressure	Helium gas at low pressure (about 10 mbar)

Table 3.1: Measuring conditions for lithium measurements at PGAA.

3.3.1 Additional Collimators

To provide an optimum beam profile and protect the setup from a beam halo, an additional collimator has been created and inserted at the end of the elliptical nose, i.e. at the place where the neutron beam enters the target chamber (see Fig. 3.5(a) - 3.5(c)). The collimator has a cubic shape and is hollow inside. The cavity has a conical shape with a rectangular cross section. Neutrons coming from the elliptical nose reach the target chamber passing through this cavity. The collimator consists of an inner shielding made from lithium doped rubbers and an outer lead shielding. The lead shielding has been designed for that scope and created by lead-pouring using the mould shown in Fig. 3.5(d). Giving the mould the desired dimensions it was possible to create a collimator perfectly fitting to the existing lead shielding at the end of the elliptical nose. The inner wall of the collimator is covered with a thin layer of a ^{6}Li enriched polymer with a thickness of about 1.5 mm, absorbing about 99.99% of the flux of neutrons in the beam halo. A fine adjustment of the beam size then occurs with help of a second collimator mounted inside the target chamber directly before the sample holder (see chapter 3.3.2).

3.3.2 Arrangement inside the Target Chamber

After passing through the lead collimator, the neutron beam coming from the elliptical nose enters the target chamber through a thin ($d = 50$ μm) Zirconium window and is further cut with help of a second collimator mounted inside the chamber. This is built from a frame of a 3 mm thick ^{6}Li enriched polymer with a rectangular shaped opening in the center. This hole has a size of $b \times h = 9 \times 14$ mm^2 [12]. The polymer is wrapped in a thin PTFE foil with the same shape, which stops alpha and tritium particles from $^6\text{Li}\,(\text{n}, \alpha)\,\text{t}$ reactions in the collimator polymer.
This additional beam shaping is necessary in order not to damage the detectors and not to activate the aluminum frame around the sample, which would considerably

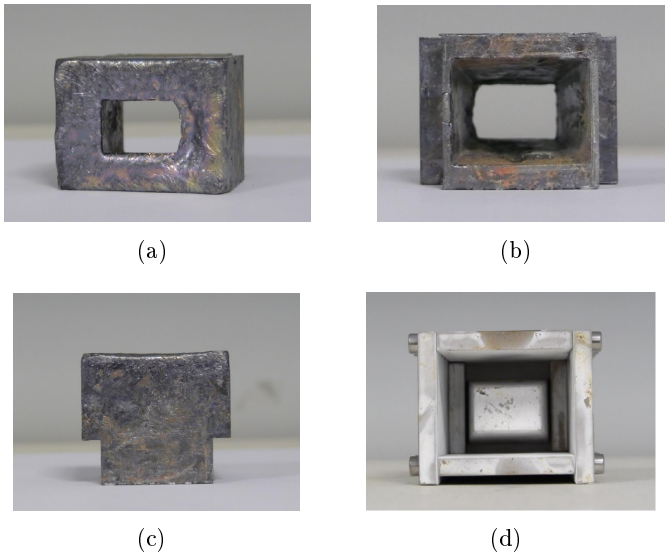

(a) (b)

(c) (d)

Figure 3.5: Photos of the fabricated lead collimator, which was inserted at the end of the PGAA elliptical nose. The inner conical surface was later covered with a 1.5 mm thick ^{6}Li enriched polymer. a: Front view. b: Back view. c: Side view. d: Mould used to cread the collimator by lead-pouring.

increase the background rate. Varying the size of the rectangular aperture in the polymer, it is possible to irradiate with neutrons a smaller or a more extended sample area according to the different experimental tasks.
The collimated beam then hits the target at an angle of 25° giving rise to the underlying nuclear reaction $^6\mathrm{Li}\,(\mathrm{n},\alpha)\,\mathrm{t}$.

3.3.3 Detector System

As shown in Fig. 2.4 a position sensitive silicon detector is mounted close to the target at a distance of $d = 20$ mm. The whole detector-target system is wrapped in a 100 μm thick PTFE foil, in order to avoid that alpha and tritium particles from the interior walls of the target chamber reach the detector. The target chamber is inwardly lined with a ^{6}Li enriched polymer which absorbs scattered neutrons.
The use of a PSD allows to simultaneously get information about the energy and the impact position of the revealed particles. Here special developed PSD detectors from Laser Components[9] had been used. With a reduced resistivity layer of 4 kΩ on

[9]Laser Components, `https://www.lasercomponents.com/de/`

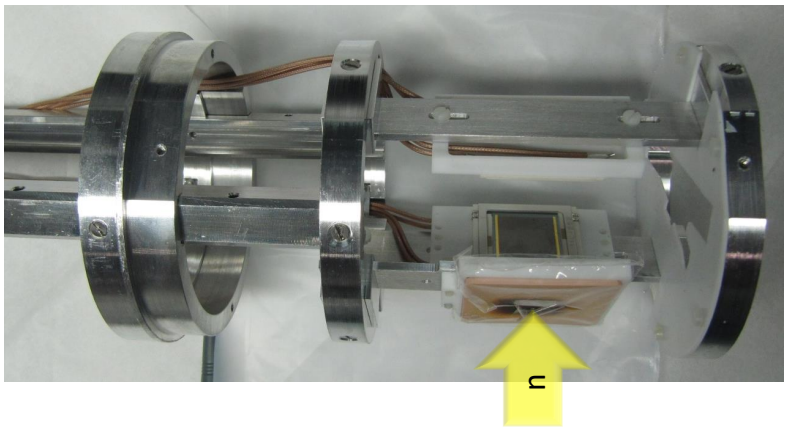

Figure 3.6: Photo of the detector setup inserted into the PGAA target chamber. The yellow arrow indicates the direction of the neutron beam. Before hitting the sample the flux field is further cut with help of a collimator made of a ^{6}Li enriched polymer, which stops the neutrons. The collimator is encased in a PTFE frame, to prevent alpha and tritium particles from (n,^{6}Li) reactions in the collimator polymer through pin holes in the PTFE frame from reaching the detector and influencing the measurement. The dark halo around the collimator aperture is due to the neutron exposure.

both sides they are optimized for this high rate application [12]. The detectors had been operated at typical background rates of $20 - 50$ kHz.
The detector size amounts to 21×21 mm^2 with an active region of 20×20 mm^2 (Fig. 3.7). Both the top and the bottom side of the silicon detector are covered by a resistive layer. When a particle hits the active region of the detector, electron-hole pairs are created and separated in the depleted volume, reaching the detector surface. Electrons and holes respectively then drift to the four contact strips at the edges of the active region. Due to the homogeneity of the resistive layer, the fraction of photocurrent split to each strip depends on the distance of the contact to the particle impact position. From the amplitude of the signal measured at each detector contact the position (x, y) where the particle has hit the detector is reconstructed.
As shown in Fig. 3.8, eight signal wires are connected to the eight contact strips of two PSDs in the coincidence setup described before. Only four of them are relevant for the experiment, since just one detector is used (see Fig. 2.4).
Those four signals from the detector are connected to a charge sensitive preamplifier (CSP) from Mesytec[10] sitting close to the target chamber (see Fig. 3.8)

[10] http://www.mesytec.com/

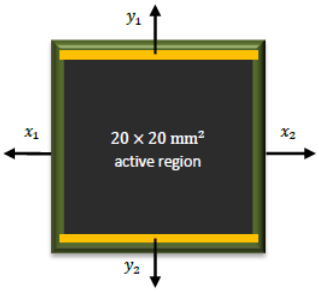

Figure 3.7: Schematic representation of the PSD used in the experiment. The detector active region amounts to 20×20 mm^2.

3.3.4 Target Ladder and Mechanics

Samples are mounted on a target ladder made of PTFE. PTFE is a good material for experiments with neutrons due to its low neutron absorption cross-section. It is a synthetic fluoropolymer consisting of carbon and fluorine, both having a very low neutron capture cross-section of $\sigma_{n,th} = 0.004$ barn and $\sigma_{n,th} = 0.010$ barn respectively [2]. Additionally, the corresponding reaction product ^{13}C is a stable isotope, whereas ^{20}F has a short half-life of 11.2 s [2] which avoids any long-lived activity in the setup.

Isotope	Natural abundance [%]	σ_n [barn]
^{12}C	98.9	0.004
^{19}F	100	0.010
^{27}Al	100	0.231

Table 3.2: Neutron capture cross-sections σ_n of the main materials used in the experimental setup [2].

On the target ladder six samples can be fixed at the same time, with help of additional target holders made of PTFE too (see Fig. 3.9). At the base of the target chamber an electric motor moves the target ladder vertically in a rail system (Fig. 3.8), driving the samples one by one to the measurement position. The motor can be controlled from the control station of the PGAA facility.
All other mechanical parts inside the target chamber like the rail system, mechanical clamps, as well as the detector interfaces are made from aluminum. Like PTFE, also pure aluminum is suitable for this kind of experiments since it has a low neutron capture cross-section of $\sigma_{n,th} = 0.231$ barn and the daughter nuclide ^{28}Al has a short half-life of 2.2 min [2].

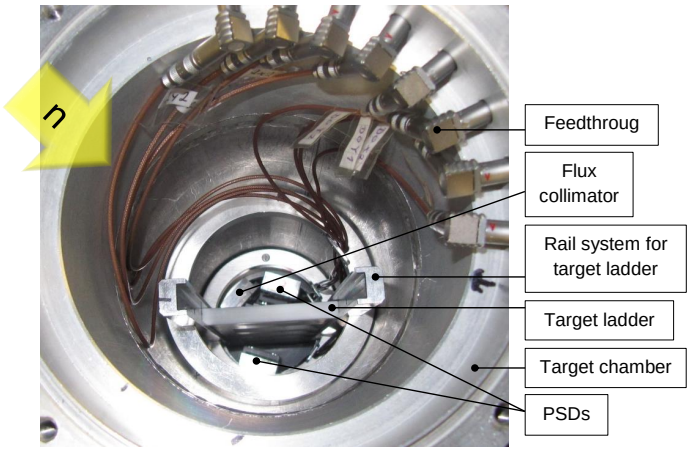

Figure 3.8: Photo of the target chamber from the top. The yellow arrow indicates the direction of the neutron beam.

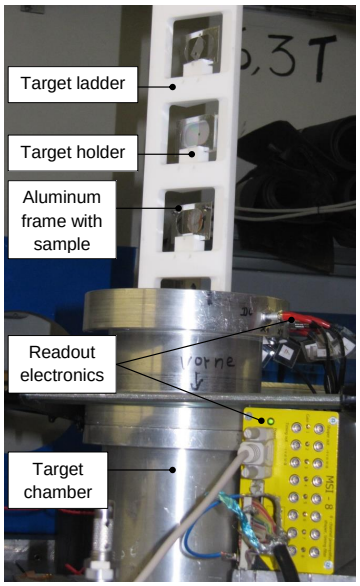

Figure 3.9: Photo of the PTFE target ladder while it is inserted into the target chamber. Six samples are fixed at the same time on the target ladder. Just one sample at a time is exposed to the neutron flux and measured. An electric motor placed at the base of the target chamber moves the ladder vertically, driving the samples one by one to the measurement position.

Chapter 4

Data Analysis

One central part of this Master thesis was the analysis of data collected during the experiment at the PGAA. In this chapter the basic concepts and the single steps of the performed analysis are presented.
The analysis process can be conceptually divided into two parts. The first one consists of a series of calibrations, which are needed to reconstruct particle impact energy and impact coordinates x and y, as well as a particle identification process, which is required to select alpha and tritium counts out of all signlas. Output of this first stage of the analysis is the reconstruction of the spatial distribution $N(x, y)$ of detected alpha and tritium particles.
In the second part of the analysis the measurement of a reference sample, having a well known lithium content, is used for a further calibration process (detector efficiency calibration and solid angle correction), as well as a reference to reconstruct the absolute lithium surface density $\lambda(x, y)$ in the analyzed target. The relative measurement between target and reference sample allows to eliminate almost all systematic errors, except mounting uncertainty and uncertainty of the lithium surface density of the reference sample. Output of this second stage of the analysis is the reconstruction of the position dependent lithium concentration $c(x, y)$ in the analyzed target.

4.1 Detector Calibration

The detector calibration is a multistep process which has to be performed in an iterative way. In a first step the four signal channels have to be roughly scaled to similar gain. This was already done online by hardware adjustment just using the hits of tritium particles from the reference sample on the readout pads of the detector, which show the largest signals on the corresponding channel. After that a raw position can be calculated according to formula 4.1. With this input the steps described in the following sections lead to a final calibration.

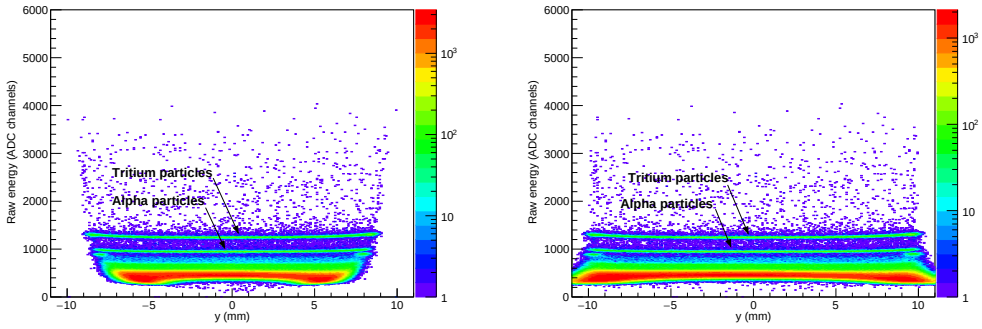

(a) (b)

Figure 4.1: a: Two-dimensional energy-position histogram from the measurement of the reference sample $RT1$ ($\lambda_{RT1} = 3\ \frac{\mu g}{cm^2}$ $^{\text{nat}}$LiF, see Chapter 6). Counts are plottet vs. ADC channels (ch) vertically and raw impact coordinate y horizontally. The tritium and the alpha line at about $\tilde{E}_t = 1300$ ch and $\tilde{E}_\alpha = 1000$ ch respectively show a slight energy dependence. Edge events are strong energy dependent.
b: Histogram in (a) after performing the offset correction; here edge events are no longer energy dependent.

4.1.1 Position Dependent Energy Calibration and Offset Correction

First of all energy calibration and offset correction are performed. Fig. 4.1(a) shows the two-dimensional energy-position histogram from the measurement of the reference target $RT1$, which has a well-known lithium surface density of about 3 $\frac{\mu g}{\text{cm}^2}$ natural lithium fluoride (see Chapter 6). Counts are plottet vs. ADC channels (ch) vertically and vs. raw impact coordinate y horizontally. Signals with uncalibrated energies smaller than about $\tilde{E} < 800$ ch correspond to background particles. The two signal lines at about $\tilde{E}_t = 1300$ ch and $\tilde{E}_\alpha = 1000$ ch arise from tritium and alpha particles from ^{6}Li reactions with neutrons. The smearing of the two lines at high energies is due to pile up with β or γ particles from the background. In Fig. 4.1(a) edge signals from particles which have hit the detector at the edges in y direction shows a strong energy dependence. This is caused by electronic offsets associated to the read-out channels. To correct this effect, electronic offsets are subtracted from the signal amplitudes before calculating particle impact positions with equation 4.1. Fig. 4.1(b) shows the energy-position histogram of Fig. 4.1(a) after performing the offset correction; y coordinates are no longer energy dependent.

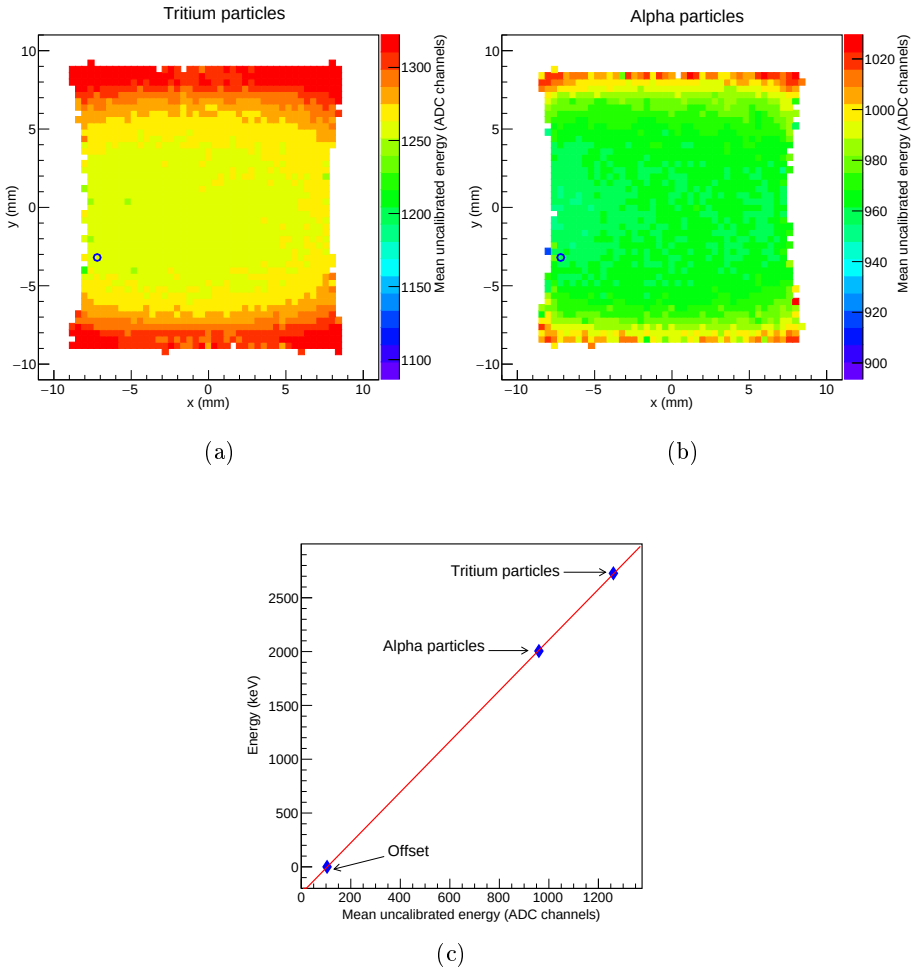

(a) (b)

(c)

Figure 4.2: Position dependent energy calibration of the measurement of Fig. 4.1.1. Fig. (a) and (b) show two-dimensional histograms where the mean uncalibrated signal amplitudes (ADC channels) from tritium and alpha particles respectively are plottet vs. particle impact coordinates x and y. Fig. (c) shows the calibration linear fit for the (x, y) position marked with a blue circle in (a) and (b) as an example.

It turns out that for this kind of measurements a standard one-dimensional energy calibration is not sufficient to correctly reconstruct particle impact energies. Indeed, due to the presence of a resistive layer on the PSD surface and to its capacitance, the rise time of signals changes depending on the particle impact position. As signal shaping time stays constant, the signal amplitude changes with the detector hit position [12]. Hence monoenergetic particles create signals with slightly different

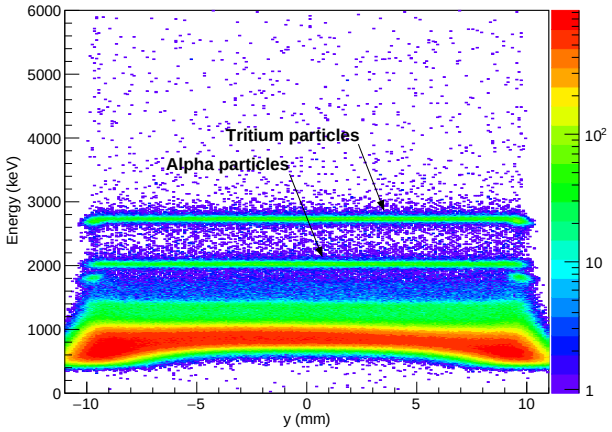

Figure 4.3: Two-dimensional energy-position histogram of Fig. 4.1(b) after performing a position dependent energy calibration. Tritium and alpha line are no longer energy dependent.

amplitudes by hitting the detector in different places.
This effect can be seen in Fig. 4.1(a), where the tritium and alpha line show a slight energy dependence. Signal amplitudes bend upwards at the edges of the detector, instead of being perfectly straight over the whole y axis, as expected.
In order to correct this effect, a two-dimensional, position dependent energy calibration is performed. The calibration process was already developed by Josef Lichtinger [12] for the analysis of similar lithium measurements in organic tissue. For details see [12].
A discrete number of "grid points" (x, y) separated by a distance of $\Delta x = \Delta y = 0.4$ mm is defined on the detector area. The average uncalibrated energy of all tritium counts lying in the neighbourhood of each grid point is calculated (see Fig. 4.2(a)). The same is done for alpha counts (see Fig. 4.2(b)). Fig. 4.2(a) and 4.2(b) show that the mean uncalibrated energy of tritium and alpha particles respectively changes depending on the particle impact position, increasing at the edges of the detector.
For each grid point (x, y) a standard linear energy calibration $E = A \cdot \left(\tilde{E} - O\right)$ is performed. Here E is the calibrated energy, $\tilde{E}$ is the mean uncalibrated energy, O corresponds to the constant offset and A to the gain parameter.
In Fig. 4.2(c) the calibration line for the grid point marked with a blue circle in Fig. 4.2(a) and 4.2(b) is shown as an example. Here the mean uncalibrated energies of tritium and alpha particles associated to the considered grid point are plottet vs. the well-known energies of tritons and alphas respectively and a linear fit is performed.

The same is done for all other grid points (x, y) defined at start.
In order to avoid discontinuity effects in the calibration, caused by the discrete number of grid points, lots of additional interstitial grid points are calculated with help of a Delauney triangulation. The corresponding calibration parameters are saved in a calibration matrix.
Fig. 4.3 shows the two-dimensional energy-position histogram of Fig. 4.1(b) after performing the position dependent energy calibration. Here the tritium and the alpha line are no longer energy dependent.
The total energy resolution of $\Delta E < 80$ keV (FWHM) is limited by the high background rate which characterizes experiments with neutrons at the PGAA station.
For the energy calibration, as well as for all other calibration and correction processes, reference measurements of samples with a well-known lithium lithium surface density are used (see Section 5.3.1 and Chapter 6).
Any change made in the detector setup during the experiment requires a new energy calibration for the following measurements, since the channel-energy association may be changed.

4.1.2 Particle Identification

In order to reconstruct lithium distributions, only signals from $^{6}\mathrm{Li}\,(\mathrm{n}, \alpha)\,^{3}\mathrm{H}$ reactions are relevant. In particular, only tritium counts are considered, since the alpha peak is contaminated by the background in most of the measurements (see Chapter 5 and 6). In order to separate tritium signals out of all counts, an energy cut is applied to the raw data.
The definition of the energy cut depends on the characteristics of the measured sample i.e. on the position and shape of the tritium peak.
Lithium measurements in very thin samples or samples containing lithium only on their surface give rise to tritium peaks with a relatively narrow width, since all tritons hit the detector with approximatly the same energy, except pile up events. This requires the definition of a relatively narrow energy cut of a few hundreds keV (see Chapter 5). Instead, by measuring thicker samples, tritium particles with a wider range of energies are detected, since they do not come only from the target surface, but also from inside the sample, typically a few μm deep (see Chapter 6). This gives rise to a rather homogeneous tritium energy distribution over a specific energy range, which requires the definition of a wider energy cut down to the next pronounced peak of the α particles.

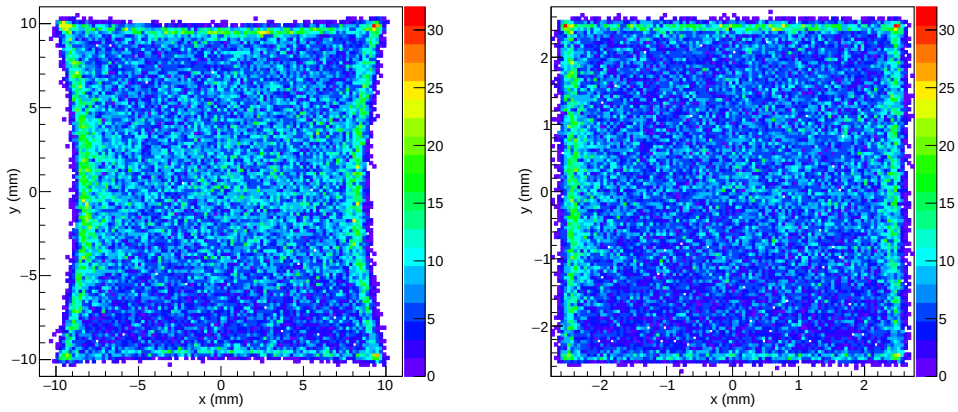

(a) (b)

Figure 4.4: Raw and calibrated two-dimensional position histogram for the measurement of the reference sample $RT1$ ($\lambda_{RT1} = 3\ \frac{\mu g}{cm^2}$ $^{\text{nat}}$LiF, see Chapter 6). Tritium counts from $^{6}\text{Li}\,(\text{n},\alpha)\,^{3}\text{H}$ reactions are plottet versus the impact coordinates x (horizontally) and y (vertically). Fig. (a) shows the uncalibrated spectrum, characterized by a pincushion deformation. Fig. (b) shows histogram (a) after performing the place calibration; the pincushion distortion has been corrected.

4.1.3 Reconstruction of Impact Coordinates and Position Calibration

Impact coordinates of particles hitting the detector are reconstructed from the signal amplitudes measured at the four detector contacts (see Chapter 3.3.2):

$$x_{det} = \frac{W}{2} \cdot \frac{E_{x_1} - E_{x_2}}{E_{x_1} + E_{x_2}} \qquad y_{det} = \frac{W}{2} \cdot \frac{E_{y_1} - E_{y_2}}{E_{y_1} + E_{y_2}} \tag{4.1}$$

E_j, $j \in \{x_1, x_2, y_1, y_2\}$, are the energies measured at each detector contact, whereas $W = 20$ mm is the detector width.
$E_{x_1} + E_{x_2} = E_{y_1} + E_{y_2} = E$ corresponds to the total energy deposited in the detector. Calculating particle impact coordinates (x_{det}, y_{det}) using equation 4.1 partially distorted results are obtained, due to the non-ideal properties of the detector. This can be clearly seen in Fig. 4.4(a), where tritium counts are plottet versus the impact coordinates x (horizontally) and y (vertically) in a two dimensional histogram. The spectrum was obtained from the measurement of the homogeneous reference sample $RT1$ ($\lambda_{RT1} = 3\ \frac{\mu g}{cm^2}$ $^{\text{nat}}$LiF, see Chapter 6). A perfectly quadratic pattern resembling the detector shape, i.e. a square of 20×20 mm^2, is expected. Instead, the pattern has a pincushion shape. In order to correct this effect, a position calibration is performed.

The distorted edges of the spectrum are fitted with second order polynomials $f_x(y) = ay^2 + by + c$ and $f_y(x) = dx^2 + ex + f$, where b and d are set to zero, as position spectra are symmetric with respect to the origin. Before filling any position histogram, spatial coordinates x and y are multiplied by the correction functions $f_x(y)$ and $f_y(x)$ respectively.
Fig. 4.4(b) shows the position histogram of Fig. 4.4(a) after performing the position calibration; the pincushion distortion has been corrected.
A further step in the position calibration is related to the presence of pinhole apertures. According to the mechanism of the camera obscura, passing through the pinhole aperture, tritons and alphas project onto the detector plane "images" of their origins, which are inverted with respect to the x and y axis (see Fig. 2.4). Moreover, the "image" of the lithium pattern which is created on the detector is enlarged with respect to the real distribution. These two factors need to be considered by reconstructing the emission position (x_{target}, y_{target}) of tritons on the target surface.
(x_{det}, y_{det}) coordinates are mirrored into $(-x_{det}, -y_{det})$, as well as scaled with the enlargement factor $\frac{b}{g}$ (see Fig. 2.2):

$$x_{target} = -x_{det} \cdot \frac{g}{b} \qquad y_{target} = -y_{det} \cdot \frac{g}{b} \tag{4.2}$$

4.2 Position Dependent Reconstruction of the Lithium Content

4.2.1 Position Dependent Lithium Surface Density

After energy calibration and offset correction a cut on the total energy for each event is performed to select the tritium impacts from the $^6\mathrm{Li}(\mathrm{n},\alpha)\,^3\mathrm{H}$ reaction (Sec. 4.1.2). Using the calculated position for each tritium impact a two-dimensional matrix $N_t(x,y)$ is derived (Sec. 4.1.3, Fig. 4.4(b)).
The distribution of tritium counts $N_t(x,y)$ is reconstructed both for the analyzed target and for a homogeneous reference sample with a well known lithium concentration. The reference run is used as "calibration scale" to determine the lithium surface density $\lambda_{sample}(x,y)$ in the analyzed target, which is calculated with the help of a simple relation:

$$\frac{N_{t,sample}(x,y)}{\lambda_{sample}(x,y)} \propto \frac{N_{t,ref}(x,y)}{\lambda_{ref}} \tag{4.3}$$

Rearrenging equation 4.3 to solve for λ_{sample}, including the normalization factors, yields:

$$\lambda_{sample}(x,y) = \frac{N_{t,sample}(x,y)}{N_{t,ref}(x,y)} \cdot \frac{t_{ref}\Phi_{ref}\kappa_{sample}}{t_{sample}\Phi_{sample}\kappa_{ref}}\lambda_{ref} \equiv \frac{N_{t,sample}(x,y)}{N_{t,ref}(x,y)} \cdot P \tag{4.4}$$

The lithium surface density in the sample is obtained by a binned scaling with the reference measurement using an additional factor P. P takes into accout the well-known durations t of both measurements as well as the respective neutron flux (Φ) settings. The additional factor κ includes the measured dead time for the data acquisition system. In equation 4.4 λ_{ref} is the well known lithium surface density of the reference sample, whereas t_{sample}, t_{ref} and Φ_{sample}, Φ_{ref} are the runtimes and neutron fluxes of target and reference measurement respectively. κ_{sample}, κ_{ref} are correction factors including lost events due to the dead time of the data acquisition. The division of position dependent number of reconstructed counts $N_{t,sample}(x,y)$ by $N_{t,ref}(x,y)$ allows to eliminate almost all systematic errors, such as any inaccuracy in the detector system or any fluctuation in the neutron flux. The position dependent detector efficiency $\epsilon(x,y)$ is also compensated through this relative measurement of target and reference sample.
Uncertainty of the lithium surface density of the reference sample and any mounting uncertainty are the only systematic errors not compensated. The same process is repeated for a background measurement, in order to reconstruct the average lithium surface density of an empty target, which is typically $\lambda_{BG} < 0.1\ \frac{\mu g}{cm^2}$. λ_{BG} is subtracted from the lithium surface density distribution of the analyzed sample.

4.2.2 Position Dependent Absolute Lithium Concentration

In order to reconstruct the position dependent absolute lithium concentration in the sample, the lithium surface density distribution $\lambda_{sample}(x,y)$ derived in Sec. 4.2.1 is normalized with the relevant sample thickness d_{max}. d_{max} indicates the maximum depth from which the tritium particles are taken into account and is determined from the maximum energy loss $\Delta E_{t,max}$ of the tritium particles, as well as from the stopping power of the sample material.
Since d_{max} is valid for tritium particles which are emitted perpendicular to the sample surface, a position dependent correction factor is introduced for tritons which are emitted under an angle α with respect to the normal to the target surface. Therefore the position dependent lithium concentration $c(x,y)$ is determined by a binned scaling of the lithium surface density distribution $\lambda_{sample}(x,y)$ with $d'(x,y,\Delta E_t) = d_{max} \cdot cos(\alpha)$.
The different steps of the data analysis described in the previous sections are summarized in Fig. 4.5.

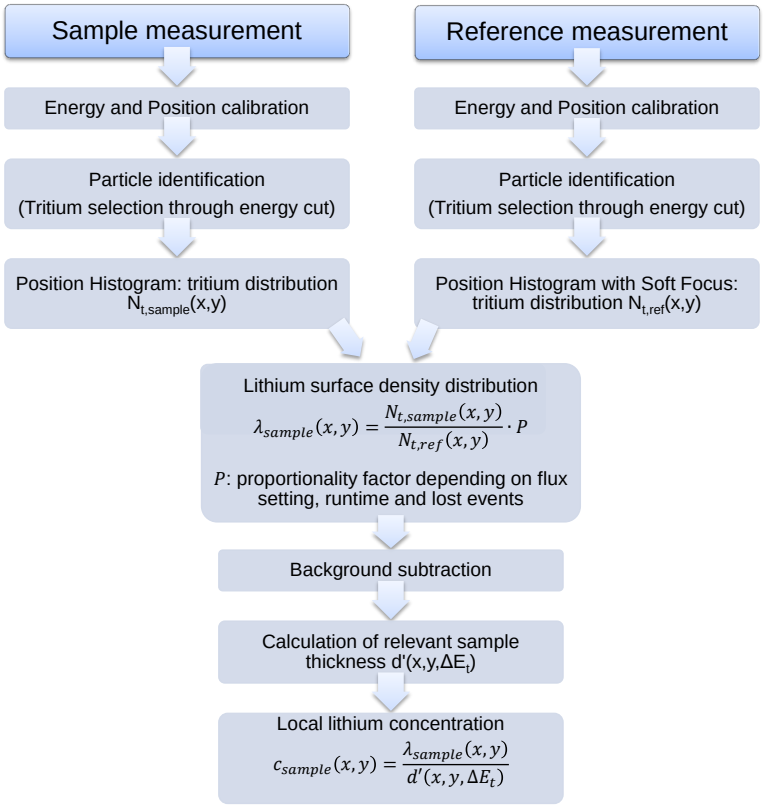

Figure 4.5: Flow diagram summarizing the main steps of the data analysis, to reconstruct microscopic lithium distributions through the relative measurement of a sample and a reference target.

Chapter 5

Lithium Measurements in TiO_2 Nanotubes

One central part of this Master thesis was the determination of lithium distributions in TiO_{2-x}-C and Si coated TiO_{2-x}-C nanotubes, electrochemically lithiated. The samples were developed in collaboration with the Material- and Nanochemistry Group led by Prof. Julia Kunze-Liebhäuser at the Institute of Physicl Chemistry in Innsbruck[1]. They were fabricated at the Institute of Physical Chemistry and transported to the PGAA facility at the FRM II to be analyzed.
The samples consist of TiO_{2-x}-C and Si coated TiO_{2-x}-C nanotubes with a length of about 1 μm, grown on Ti substrates and loaded with lithium ions (see Chapter 5.1). The lithiated TiO_{2-x}-C nanotubes on the titanium substrate are chemically activated and have to be kept in an inert environment. For example, if they come into contact with air, oxygen molecules interact with the material and cause oxydation, damaging the samples.
Therefore one of the first priorities preparing the experiment was to develop a method to keep the nanotubes samples in inert gas during all stages of the experiment, from the fabrication in Innsbruck to their measurement in Garching.
After their fabrication the nanotubes samples were sealed in special mini-containers; design and fabrication of the mini-containers will be described in Chapter 5.2. For the transport to the FRMII the mini-containers were put in small tubes filled with purified argon gas. Inside the FRMII they were stored in a glove box with argon atmosphere, until they were mounted onto the target ladder of the PGAA setup. Before starting any measurement the PGAA target chamber was evacuated and the chamber was continuously flushed with helium at a pressure of about 10 mbar, to purge any remaining nitrogen or oxygen out the chamber, creating an inert environment for the samples.

Two batches of samples, characterized by non-coated and Si coated TiO_2 nanotubes respecitively, with different lithium contents, were analyzed. For each sample the position dependent lithium surface density was reconstructed using the analysis process described in Chapter 4. Some of the most relevant results will be presented

[1] http://www.uibk.ac.at/physchem/materials-nanochemistry/

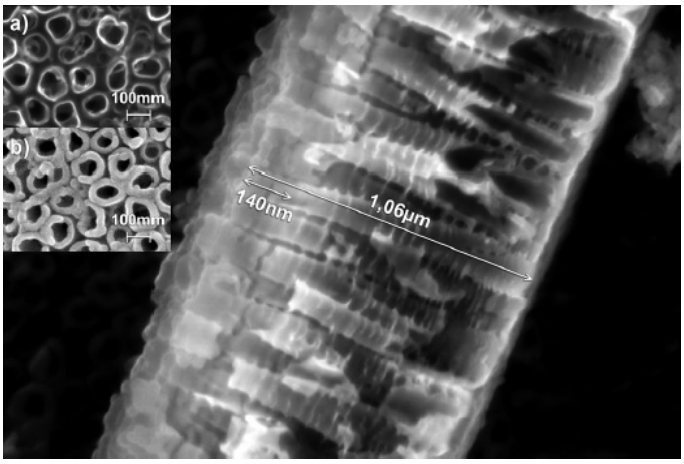

Figure 5.1: SEM image of TiO_{2-x}-C nanotubes coated with silicon, fabricated by the Material- and Nanochemistry Group at the University of Innsbruck. The nanotubes are covered by a ~ 10 nm thick silicon coating for 140 nm of their top length, both at the inner and the outer side. Inset a): top view of non-coated TiO_{2-x}-C nanotubes. Inset b): top view of TiO_{2-x}-C nanotubes coated with silicon. Source: [8].

and discussed in the second part of this chapter (see Chapter 5.3).
Electrochemistry also gives information about the total amount of lithium in the nanotubes samples. In collaboration with the Material- and Nanochemistry Group at the Institute of Physicl Chemistry in Innsbruck results from the electrochemistry and from the PGAA measurements were compared (see Sec. 5.3.2 and Sec. 5.3.3).

5.1 Sample Fabrication

Two different types of samples were investigated. The first batch (12 samples) consists of self-organized TiO_{2-x}-C nanotubes, anodically grown on titanium substrate and charged with lithium ions. Mechanically polished titanium disks with a native oxide layer on the top surface were used as substrate. The disks have a thickness of $t = 1$ mm and a diameter of $D = 20$ mm. The TiO_2 nanotubes were grown by electrochemical anodization in electrolyte containing fluoride, by applying an anodic potential of 20 V for 1 h [18]. Inset (a) of Fig. 5.1 shows a SEM image of the nanotubes from a top view. The nanotubes have an average length of about 1 μm, an average wall thickness of about 18 nm and an average outer tube diameter of about 100 nm [18]. An increased potential of 60 V (for 2 h) was applied to one of the samples, in order to grow longer nanotubes with a length of about 4 μm.
The as grown amorphous TiO_2 nanotubes were then annealed at 400°C in an Ar/C_2H_2 mixture, converting their structure from amorphous to anatase and form-

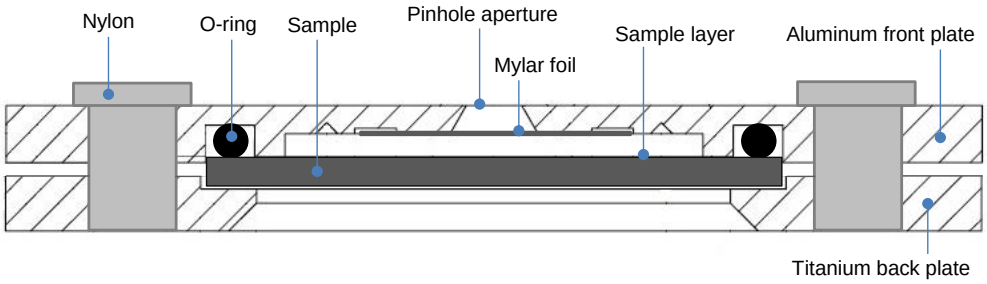

Figure 5.2: Schematic representation of the mini-container for TiO_2 nanotubes samples.

ing a thin carbon layer at the outer wall of the tubes. The carbon coating enhances the electronic and ionic conductivity of the nanotubes and therefore their capacity to incorporate lithium ions. For further details about the sample fabrication see [18].
The second batch of samples (5 samples) consist of $TiO_{2\text{-}x}$-C nanotubes coated with a thin film of silicon ($\sim$ 10 nm), which covers about 140 nm of the nanotubes length, both at their inner and outer wall (see Fig. 5.1). Silicon has an extraordinary high lithium storage capacity of 3580 $mAhg^{-1}$ [19] at room temperature and a low lithiation/delithiation voltage of $\sim 0,5$ V vs. Li/Li^+, which make Si one of the most promising anode materials for lithium-ion batteries [8]. For further details about the fabrication of silicon coated $TiO_{2\text{-}x}$-C nanotubes see [8].
The fabricated titanium dioxide nanotubes were used as anode material in Li-ion cells. Lithiation and delithiation of the nanotubes were performed in a three electrode setup inside an electrochemical cell. The cell was mounted inside a glove box under argon atmosphere, in order to keep the nanotubes in an inert environment (see [18] and [8]).

5.2 Design and Fabrication of Mini-Containers for the Nanotubes Samples

Designing the mini-containers for the nanotubes samples, the following list of requirements should be fulfilled:

- Gas tightness;
- Free space of a couple of millimeters should be left between sample and front

side of the container, since this should not come into contact with the sample surface, in order not to damage the nanostructures;

- Samples should be kept perfectly fixed inside the mini-containers;
- Since mini-containers are exposed to the neutron beam together with the nanotubes samples inside, they should be made of materials having a low neutron capture cross-section and their reaction products after neutron activation should have short decay times. Otherwise the presence of the mini-containers would dramatically increase the background in the measurements or the waiting time before accessing the samples, after switching off the neutron beam;
- Relatively small size of the mini-containers. Objects with a maximum size of about $40 \times 40 \times 40$ mm^3 can be introduced into the PGAA target system (see Chapter 3.3.2);
- Manually opening and closing of the mini-containers should be fast. This is helpful during fabrication or in case of urgent changes during the experiment;
- For position dependent measurements using the technique of the camera obscura, a pinhole aperture should be integrated in the structure of the mini-containers.

Pure aluminum and pure titanium have been chosen as materials for the mini-containers. Their low neutron capture cross sections and short decay times make them particularly suitable for experiments with neutrons [2].
Two metallic circular plates held together by seven Nylon screws form the mechanical frame of the mini-containers (see Fig. 5.2 and 5.3). The back plate (see Fig. A.2) is made of 5.6 g pure titanium, whereas the front plate (see Fig. A.1) is made of 3.8 g pure aluminum. Both plates have a thickness of $h = 2$ mm and an outer diameter of $D = 35$ mm.

The basic idea behind the design of the mini-containers is using the sample substrate as a sealing part. The sample is placed between the front and the back plate of the mini-container. Pressing the two plates one against the other, a seal is created at the sample-plate interfaces due to the presence of an O-ring, a loop of elastomer with a round cross-section and the shape of a torus (see Fig. 5.2). The O-ring has the function of mechanical gasket: when a pressure is applied to the front and back plate, the O-ring is compressed and creates a seal at the interfaces, making the mini-container gas tight. To create a sufficient mechanical pressure the Nylon screws are used. According to the design of the mini-containers, the right pressure is created when the screws are tightened until getting a spacing of exactly 500 μm between front and back plate.

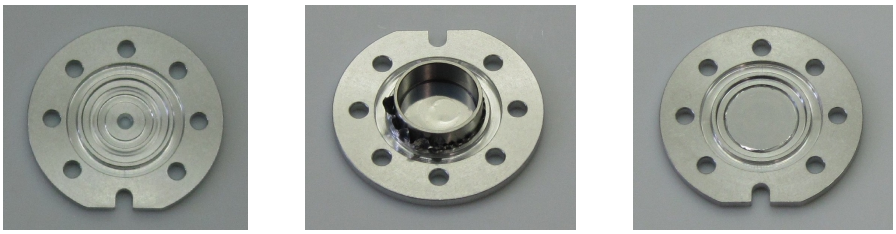

(a) (b) (c)

Figure 5.3: Pinhole aperture and window production in the mini-containers for TiO_2 nanotubes samples.
a: Front aluminum plate of the mini-container.
b: A stainless steel ring is used to stretch a 2 μm thick Mylar foil during the gluing process to the aluminum plate.
c: Final state of the front aluminum plate with the Mylar foil fixed to the plate and sealing the circular opening.

5.2.1 Pinhole Apertures Production

The front aluminum plate of the mini-container has a circular opening of diameter $d = 2$ mm in the center (see Fig. 5.3(a)), so that the detector-mini-container system acts as a camera obscura for the nanotubes sample.
The circular aperture needs to be sealed by an extreme thin foil, to minimize energy losses of tritium and alpha particles coming from $^6\mathrm{Li}\,(\mathrm{n},\alpha)\,^3\mathrm{H}$ reactions occurring in the lithiated nanotubes by exposure to the neutron beam.
The apertures were sealed with a 2 μm thick Mylar foil, coated on both sides with aluminum layers of 250 nm thickness (see Fig. 5.3(c)). The foil is thick enough to make the mini-containers gas tight. At the same time it causes relatively small energy losses to tritium and alpha particles. Passing through the Mylar window, tritons with an energy of about $E_t \approx 2.7$ MeV typically lose about 3% ($\Delta E_t \approx 70$ keV), whereas alphas with an energy of about $E_\alpha \approx 2.1$ MeV lose about 20% ($\Delta E_\alpha \approx 400$ keV) of their kinetik energy.
The complicated structure of the aluminum front plate, with a series of concentric cavities and grooves (see Fig. A.1), was designed to fix the Mylar foil to the plate by epoxy adhesive[2].
Using an optical microscope the status of the Mylar window and of the pinhole aperture was checked for each fabricated mini-container. The following requirements should be fulfilled:

[2] UHU® plus endfest 2-K-Epoxidharzkleber (2-component epoxy resin adhesive for heavy-duty requirements), `www.uhu.com`

- The aluminum foil should be perfectly streched, without any wrinkle, crack or microgap;
- The foil should perfectly adhere to the plate at any point along the perimeter of the pinhole aperture;
- There should not be any trace of the epoxy resin adhesiv used to fix the foil to the plate inside the pinhole aperture, since this would stop tritum and alpha particles.

5.2.2 Optical Quality Control and Leak Test

The tightness of each fabricated mini-container was checked using an optical method, in order to exclude the presence of any microscopic crack or hole in the Mylar foils, which could let oxygen molecules enter the mini-containers. In the following paragraph the method used for this test measurements is briefly described.
The mini-containers encase very small volumes of about $V = 0,3$ cm^3, which makes several common leak test techniques not suitable. Helium leak test was also not suited, since Mylar foils have a normal leak rate for Helium. Therefore an optical method was used.
The mini-containers are placed into a vacuum chamber, exactly below a small "window" of transparent glass which lets light enter the chamber. A red laser is mounted above the vacuum chamber at a distance of about $d = 30$ cm, so that the light points exactly to the Mylar foil. A white screen made of papar is mounted around the laser (see Fig. 5.2.2). The aluminum coating of the foil reflects the light creating an image on the white screen. Observing the evolution of the light pattern when the vacuum chamber is evacuated and then ventilated again, static conditions of the Mylar foil are determined.
Evacuating the chamber the Mylar foil bends upwards, since the pressure of air on the inner side of foil is no longer compensated by a pressure from the outer side, which gives rise to a broader light pattern. Then, if the mini-container is gas tight, the foil goes back to the initial configuration when the chamber is ventilated after one or more hours and the starting image is observed on the screen. Otherwise, since air has left the box, the Mylar foil bends downwards and a still different light pattern is observed.

5.3 Data Analysis and Discussion

Tritium detection analyis was successfully used to reconstruct the litihum content in self-organized TiO_{2-x}-C and Si/TiO_{2-x}-C nanotubes electrochemically lithiated.

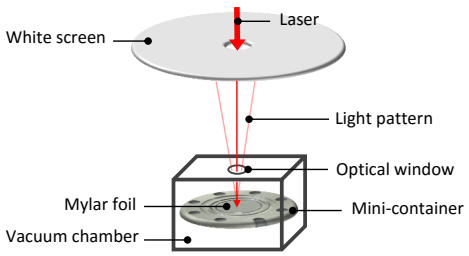

Figure 5.4: Schematic representation of the setup used for the optical leak tests in the mini-containers for TiO_2 nanotubes samples.

The position dependent lithium surface density on a 2×2 mm^2 target area was reconstructed for about 17 samples. The analysis process based on the detection of tritium particles is described in detail in Chapter 4. For a few nanotubes samples a larger target region of about 11×8 mm^2 was additionally analyzed, allowing to resolve any inhomogeneities in the lithium distribution over a larger sample area.
Some samples show a homogeneous lithium surface density over the investigated area, whereas inhomogeneities in the lithium content are observed in a few samples, which show regions with a much higher lithium surface density than others. This is probably related to full lithiation of $Li/TiO_2 \approx 0.9$ only on certain areas, which are called "hot spots" [20].
In section 5.3.1 the analysis of a reference measurement is presented, whereas in section 5.3.2 and 5.3.3 the reconstruction of the local lithium surface density in two of the investigated samples, characterized by TiO_{2-x}-C and Si/TiO_{2-x}-C nanotubes respectively, is shown. In both samples the nanotubes have a length of about 1 μm and were electrochemically lithiated (see section 5.1). The first sample shows a rather homogeneous lithium surface density, whereas the second one shows local variations in the lithium content. Reasons for this inhomogeneity are currently investigated.
The analysis of a third sample, characterized by longer TiO_{2-x}-C (with a length of about 4 μm), is presented in section 5.3.4.

5.3.1 Reference Measurement

In this section the analysis of a reference measurement - used for the calibration of the detector system (see Chapter 4.1), as well as a reference to determine the absolute lithium content in the TiO_{2-x}-C and Si/TiO_{2-x}-C nanotubes samples (see Chapter 4.2.1) - is discussed. The reference target ($RT2$) consists of a 1 mm thick titanium round disk with a diameter of 20 mm, the same as those used as substrate for the

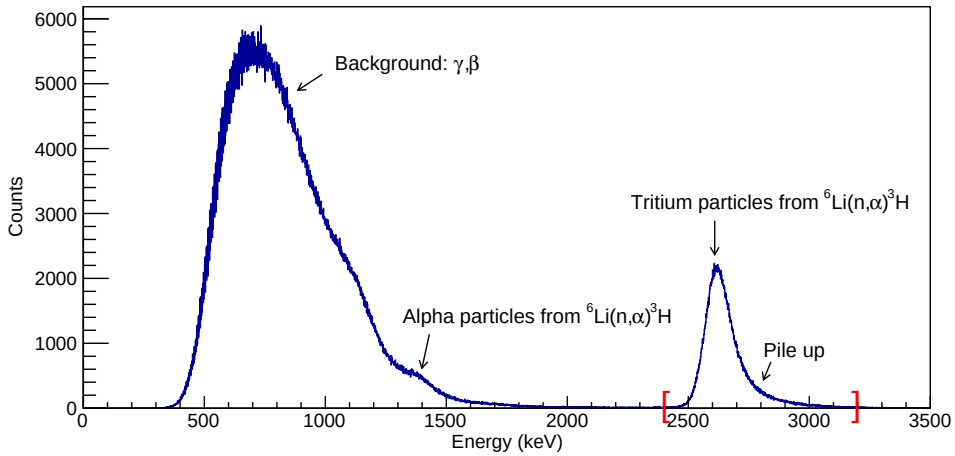

Figure 5.5: Energy spectrum of the reference target $RT2$ ($\lambda = 50\ \frac{\mu g}{cm^2}$ ^{nat}LiF). Red brackets represent the applied energy cut.

titanium dioxide nanotubes, sealed in a mini-container. On the polished surface of the titanium disk a well known amount of natural lithium fluoride ($\lambda_{ref} = 50 \pm 1\ \frac{\mu g}{cm^2}$ ^{nat}Li) was homogeneously deposited by thin film deposition[3]. $RT2$ was measured at a flux of cold neutrons of about $\Phi = 4.59 \cdot 10^8\ \frac{n}{cm^2 s}$ over a runtime of $t = 3855$ s. Fig. 5.5 shows the energy spectrum from the measurement of $RT2$. At small energies the spectrum is dominated by background signals, mainly from γ and β particles, created dominantly in the large mass of the mini-container. The background distribution is cut on the left side by the trigger threshold of the data acquisition, and decreases exponentially on the right side. On the right tail of the background distribution (see Fig. 5.5) a further feature can be recognized at about 1440keV, corresponding to the right edge of the distribution of alpha particles from the neutron capture reaction by lithium-6. Alpha particles are emitted with an energy of about 2055 keV and lose about 600 keV by passing straight through the Argon gas inside the mini-container and the Mylar window; the ladder one causes the most part of the energy loss (about 400 keV). At high energies the spectrum is dominated by tritium signals from $^6\mathrm{Li}\,(\mathrm{n},\alpha)\,^3\mathrm{H}$ reactions. The tritium peak sits at about $E_t = 2630$ keV and shows a right tail corresponding to pile up with particles from the background. Tritium particles from ^{6}Li reactions with neutrons are emitted from the surface of the homogeneously lithiated titanium disk inside the mini-container with an initial

[3]Target laboratory of the ZTL (Zentrales Technologie Labor), Department of Physics, Technische Universität München.

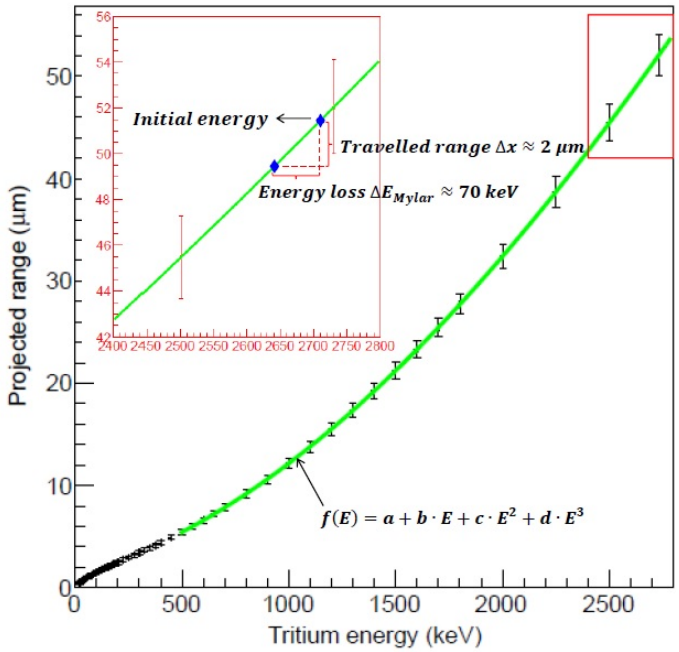

Figure 5.6: Reconstruction of the energy loss of tritium particles in 2 μm Mylar ($\rho_{Mylar} = 1.397\ \frac{g}{cm^3}$) using SRIM[4]. Projected ranges are plottet versus tritium energy. Points are fitted with a polynomial function of the form $f(E) = a + b \cdot E + c \cdot E^2 + d \cdot E^3$, which shows that tritium particles lose about $\Delta E_{t,Mylar} = 70$ keV while passing through 2 μm Mylar.

energy of $E_t = 2727$ keV. Before hitting the detector, tritons lose part of their energy (about $\Delta E_t = 100$ keV) passing through several layers of material:

- Argon gas. Tritons travel about 1 mm inside a small volume in the mini-container, which is filled with argon gas, and lose about $\Delta E_{t,Ar} = 30$ keV.
- Mylar[5]. Tritium particles lose about $\Delta E_{t,Mylar} = 70$ keV while passing through the 2 μm thick Mylar foil sealing the pinhole aperture of the mini-container.
- Helium gas. Tritons travel about 20 mm inside the target chamber, which is filled with helium gas at a pressure of about $P = 10$ mbar. The low pressure minimizes the energy loss of tritium particles (below 1 keV), which can be neglected.

[4]SRIM - The Stopping and Range of Ions in Matter `http://www.srim.org/`
[5]Polyethylene terephthalate $(C_{10}H_8O_4)_n$

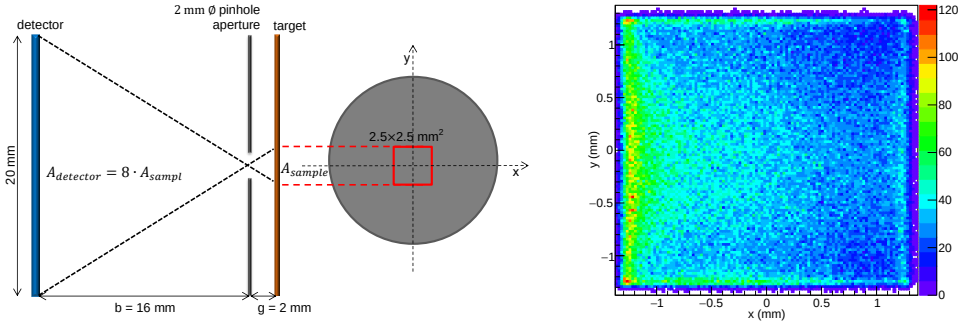

(a) (b)

Figure 5.7: a: Schematic representation of the experimental setup used for the lithium measurement in titanium dioxide nanotubes.
b: Two-dimensional tritium distribution in the reference target $RT2$. Due to a magnification factor of $\frac{b}{g} = 8$, a sample area of 2.5×2.5 mm^2 was investigated.

Energy losses were calculated from the stopping power of the different materials using SRIM[6]. As example the reconstruction of the energy loss in the 2μm thick Mylar foil is shown in Fig. 5.6. This shows the stopping power of ^{3}H particles in Mylar. For a descrete number of tritium energies (plottet on the x axis) the corresponding depths in μm to which ^{3}H particles penetrate in the course of slowing down to rest are plottet on the y axis. This descrete number of data points from SRIM is fittet with a polynomial function of the form $f(E) = a + b \cdot E + c \cdot E^2 + d \cdot E^3$, in order to associate a projected range to all tritium energies between $E_{t,min} = 500$ keV and $E_{t,max} = 2727$ keV. From the difference in the projected ranges corresponding to the tritium energy before and after passing the Mylar window, the energy loss of the particles by going through the 2μm thick Mylar foil is reconstructed; it amounts to about $\Delta E_{t,Mylar} = 70$ keV.

Since alpha particles can not be clearly separated from the background - this is the case also for the measurements of the TiO_2 nanotubes samples (see Fig. 5.10(a)) - only tritium signals were used in the analysis to reconstruct the lithium content. To perform the energy calibration (see Chapter 4.1.1) only tritium signals and energy offset were used. Also in the further steps of the analysis only ^{3}H counts were considered. Red brackets in Fig. 5.5 show the energy cut which was applied to the raw data of all measurements, in order to separte tritium signals from all counts. The cut was defined between $E_{t,min} = 2400$ keV and $E_{t,max} = 3200$ keV. This energy upper limit is not physical but results from pile up. However, as there are no high

[6]SRIM - The Stopping and Range of Ions in Matter, `http://www.srim.org/`

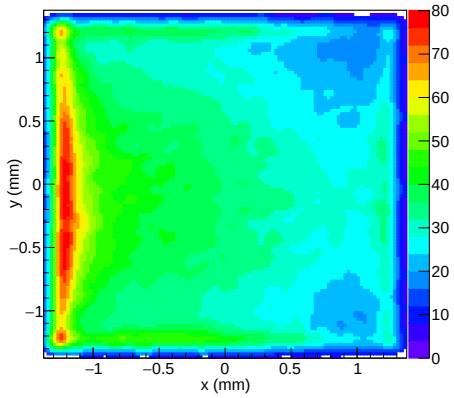

Figure 5.8: Tritium distribution of Fig 5.7(b) after applying a soft focus filter with gaussian distributed weights with a sigma of $\sigma_{sf} = 40$ μm, in order to compensate statistical fluctuations.

energy charged particles expected in this energy regime, all counts in the tritium peak can be attributed to tritons from the $^{6}\mathrm{Li}\,(\mathrm{n},\alpha)\,^{3}\mathrm{H}$ reaction.

5.3.1.1 Definition of a reference matrix for normalization

Fig. 5.7(b) shows the two-dimensional tritium distribution $N_{t,ref}\,(x,y)$ from the measurement of the reference target, which was used to normalize the sample measurements. Selected tritium counts are plotted versus their emission coordinates x and y. Due to an enlargement factor of $\frac{b}{g} = 8$, caused by the presence of the pinhole aperture (see Chapter 5.2.1), a target region of 2.5×2.5 mm^2 was investigated (see Fig. 5.7(a)). A gradient in x direction can be observed, with more entries in positive x-direction than in the negative one, although an approximately constant number of tritium entries should be observed throughout the target area, since the reference target has a homogeneous lithium surface density. The observed gradient is attributed to flux inhomogeneities of the neutron beam.
Fig. 5.8 shows the position histogram of Fig. 5.7(b) after applying a soft focus filter with normalized gaussian distributed weights, in order to compensate statistical fluctuations. The gaussian blurring algorithm replaces each histogram bin's value with the weighted average of that bin's neighbourhood. The original bin's value receives the highest weight, whereas neighbouring bins receive smaller weights as their distance to the original bin increases. A neighbourhood of size $x = y = \pm 0.2$ mm was chosen, in order to have a significant number of entries in each matrix bin. This corresponds to a standard deviation of the gaussian filter of about $\sigma_{sf} = 40$ μm. To take into account the discontinuity at the edges of the detector, a condition for

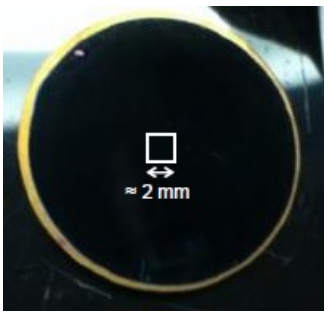

Figure 5.9: Photo of Sample 3 (see Table B.1) - charachterized by self-organized TiO_{2-x}-C nanotubes, anodically grown on titanium substrate - after lithiation. The white rectangle qualitatively shows the measured area. Original photo from [20].

the soft focus algorithm was applied, for a significant number of filled bins for the averaging. Only if the sum of the weights of the filled bins corresponds to at least 20% of the maximal matrix weight, the filter is applied. This condition ensures that the soft focus algorithm stops at the outer border of the histogram.
The spatial resolution of the measurement is given by $\sigma = \sqrt{\sigma_i^2 + \sigma_{PA}^2}$. σ_i corresponds to the intrinsic spatial resolution of the detector, which amounts to about 300 μm, whereas $\frac{\mathrm{D}}{\sqrt{12}}$ is assumed as contribution of the pinhole aperture σ_{PA} (D corresponds to the aperture diameter and is equal to about 2 mm). This gives rise to an effective spatial resolution of the measurement of about $\sigma_{eff} \approx 0.65$ mm.

5.3.2 Lithium Measurement in TiO_{2-x}-C Nanotubes

In this section the local lithium surface density in one of the investigated samples (Sample 3 in Table B.1) is discussed in detail (see Fig. 5.9). This sample was fabricated according to Sec. 5.1 with rather short tubes of 1 μm length. The sample is characterized by self-organized TiO_{2-x}-C nanotubes, electrochemically lithiated through galvanostatic cycling with potential limitation at 1.1 V vs. Li/Li^+ [18].
The sample sealed in a mini-container was measured with a flux of cold neutrons of about $\Phi = 4.59 \cdot 10^8 \frac{\mathrm{n}}{\mathrm{cm^2 s}}$ over a runtime of about 900 s. Fig. 5.10(b) shows the calibrated two-dimensional energy-position histogram from the sample measurement to illustrate the selection criteria for the further analysis.
After the event selection in both the sample and the reference target the absolute and relative lithium concentrations could be determined for different spatial filter sizes as shown in Fig. 5.11. Fig. 5.11(a) shows the tritium distribution in the sample, after applying a gaussian blurring algorithm (see Sec. 5.3.1.1) with a standard deviation

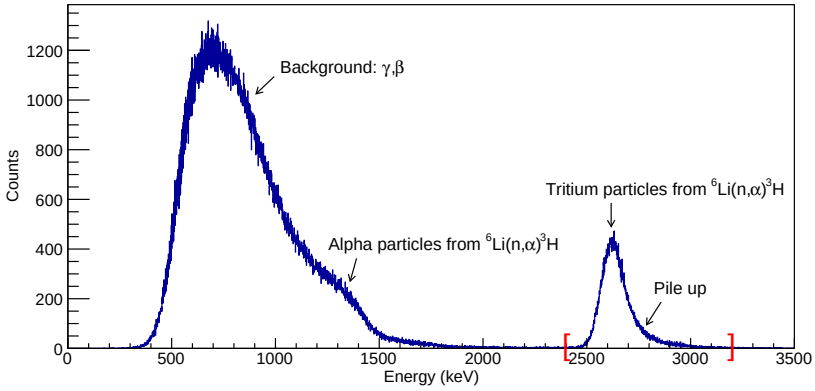

(a)

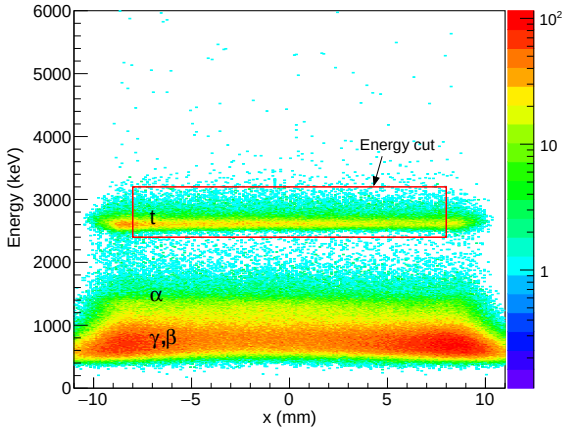

(b)

Figure 5.10: Data from the measurement of Sample 3 (TiO_{2-x}-C nanotubes, see Table B.1). Fig. (a) shows the energy spectrum. In the two-dimensional histogram of Fig. (b) counts are plottet versus calibrated energy (vertically) and versus impact coordinate x (horizontally). The red brackets in Fig. (a) and the red rectangle in Fig. (b) represent the energy cut applied to select tritium signals.

of $\sigma_{sf} = 40$ μm - the same as used for the reference target - in order to compensate statistical fluctuations.
The result of this steps (see Fig. 5.11(a)) is then normalized by the measured distribution for the reference sample and scaled by the corresponding factor P (see Sec. 4.2.1), to obtain the lithium surface density in the sample (see Fig. 5.11(b)).

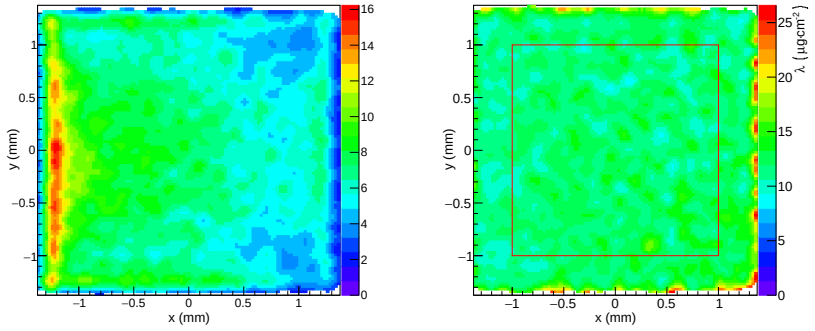

(a) (b)

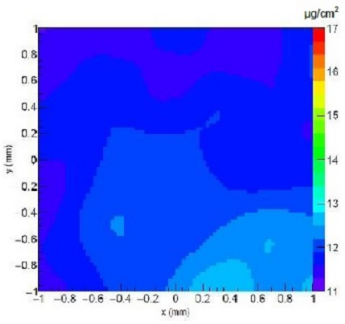

(c)

Figure 5.11: Position dependent tritium distribution (a) and local lithium surface density (b) in Sample 3 (TiO_{2-x}-C nanotubes, see Table B.1). The red square represents the cut which was applied in order to exclude signals from the edges of the detector. Fig. (c) shows the histogram in (b) after application of a more extended soft focus filter; here ony the area within the red cut is shown.

The sample shows a homogeneous lithium content over the investigated electrode area, as expected from electrochemistry. The large diameter of the pinhole aperture ($\approx$ 2 mm) limits the saptial resolution of the measurement. Therefore fluctuations in the lithium surface density which are observed in Fig. 5.11(b) on a spatial scale of about 0.05 mm do not have a physical origin, but are rather statistical fluctuations. Especially fluctuations at the borders of the sensitive area are due to discontinuities not properly handled by the algorithm. The homogeneity of the sample is more evident in Fig. 5.11(c), which shows the histogram of Fig. 5.11(b) after applying a further soft focus filter with a larger standard deviation corresponding to the spatial resolution of $\sigma_{xy} \sim 0.65$ mm achieved by the limit of the setup.
The average lithium surface density in the sample is equal to $\lambda = 11.83 \pm 1.47 \ \frac{\mu g}{cm^2}$;

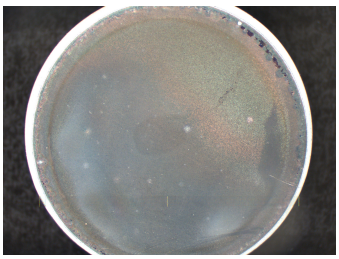

Figure 5.12: Optical image of Sample 10 (see B.1) - characterized by self-organized Si/TiO_{2-x}-C nanotubes, anodically grown on titanium substrate - after lithiation.

it was calculated over a reduced target area of about 2×2 cm^2 (see red cut in Fig. 5.11(b)) - which corresponds to a reduced detector area of about 16×16 mm^2 - in order to exclude signals from the edges of the detector.
From electrochemistry a lithium content of $\lambda_{EC} = 11.42 \pm 1.43$ $\frac{\mu g}{cm^2}$ [20] is obtained, measuring the electrochemical charge upon lithiation/delithiation for the same electrode. Both results agree within the uncertainty intervall.

5.3.3 Lithium Measurement in Si/TiO_{2-x}-C Nanotubes

In this section the measurement of one of the investigated samples containing silicon (Sample 10 in Table B.1) is presented for comparison. Self-organized titanium dioxide nanotubes were grown on titanium substrate; they have a length of about 1 μm and an outer diameter of about 100 nm. The nanotubes were additionally coated with a thin film of silicon (about 10 nm) and electrochemically lithiated through galvanostatic cycling with potential limitation (see Sec. 5.1 and [8]). Fig. 5.12 shows an optical image of the sample after lithiation. The sample was measured both from inside the mini-container and in "open-setup". For the measurement in open-setup the titanium plate was fixed on a target frame made of pure aluminum with a thickness of about 300 μm. It was measured with a flux of cold neutrons of about $\Phi = 2.72 \cdot 10^8$ $\frac{n}{cm^2 s}$ over a runtime of about 600 s. A Teflon[7] foil with a thickness of about 100 μm, stopping alpha and tritium particles, fixed on a pure aluminum frame was used as pinhole aperture. A hole with a diameter of about 2 mm was cut into the foil with a stamp tool. The pinhole aperture was placed in the middle between target and detector at a distance of about 10 mm both from the target and from the detector, resulting in a magnification factor of 1, i.e. a map of the lithium pattern in the sample was created onto the detector plane in a 1:1 scale. Measurements in open-setup allow to investigate a much larger electrode area of about 11×8 mm^2. For the measurement in open-setup the samples had to be

[7] Teflon™

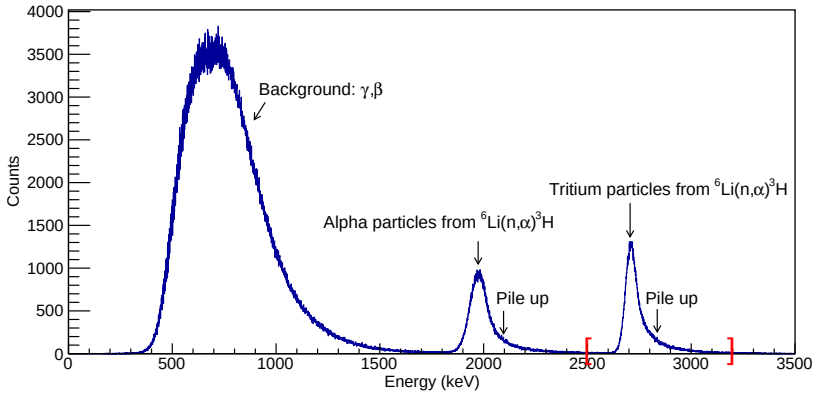

Figure 5.13: Counts vs. calibrated energy spectrum for a reference titanium disk with a well-known lithium surface density. The target was measured in "open setup".

removed from their mini-containers and were handled in air for about five minutes. During that time they were fixed on aluminum frames and mounted onto the target ladder (see Fig. 3.9), together with the pinhole apertures. The target ladder was then inserted into the target chamber, where the inert environment was created again. Although the first priority by the open-setup measurements was to minimize the time in which the nanotubes might come into contact with air, the oxydation of even tiny amounts of the electron material due to the oxygen molecules can not be excluded, which of course represents a disadvantage of the open-setup configuration. Fig. 5.13 shows the calibrated energy spectrum from the measurement of the reference target RT2 measured in open setup. In this configuration tritium and alpha particles from the neutron capture reaction by lithium-6 do not pass through any material layer - as it was the case for the mini-container configuration - and lose only a negligible amount of energy due to collisions with helium molecules inside the target chamber, hitting the detector with approximately their emission energies (2.7 MeV and 2.1 MeV respectively - see Sec. 2.1).
Fig. 5.14 shows the local lithium surface density in $\frac{\mu g}{cm^2}$ in the silicon sample. The histogram in Fig. 5.14(a) shows the entire investigated electrode area, only limited by the size of the neutron beam. A reduced region of about 11×8 mm^2 is shown in Fig. 5.14(b), in order to exclude signals from the edges of the detector. The average lithium surface density in the sample is calculated over this reduced area and amounts to $\lambda = 17.68 \pm 2.27$ $\frac{\mu g}{cm^2}$, which agrees within the error intervall with the electrochemical charge calculated upon lithiation for this sample ($\lambda_{EC} = 15.46$ $\frac{\mu g}{cm^2}$ [20]). The sample shows a rather inhomogeneous lithium surface density, with some regions containing much more lithium than others. For example region 1 in Fig.

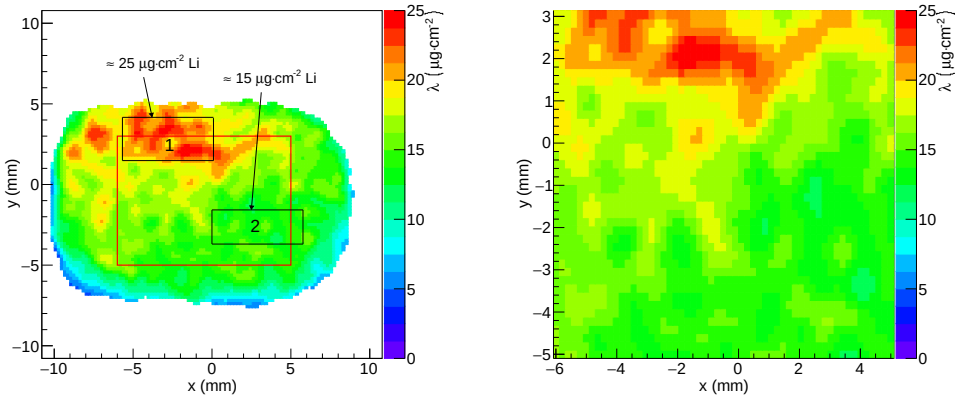

(a) (b)

Figure 5.14: Local lithium surface density in Sample 10 (Si/TiO_{2-x}-C nanotubes electrochemically lithiated, see Table B.1), measured in "open setup" configuration. In Fig. (a) the whole electrode area is shown, whereas a zoom over the region within the red cut is shown in Fig. (b), in order to exclude signals from the edges of the detector.

5.14(a) shows about 65% more lithium than region 2. Possible explanations for this inhomogeneity are currently investigated by our collaboration partners from the Material- and Nanochemistry Group[8] led by Prof. Julia Kunze-Liebhäuser.
SEM images of the sample not presented here [20] show that there are no differences in the geometry of the nanotubes in region (1) and (2), so that the local variation in the lithium surface density can not be explained by an inhomogeneous growth of the nanotubes.
It can probably be related to the presence of so called "hot spots" i.e. regions of the electrode where the TiO_{2-x}-C nanotubes are fully lithiated (second phase transition). Region (1) may be a hot spot, since the average lithium surface density in this area ($\lambda_1 \approx 25\ \frac{\mu g}{cm^2}$) corresponds to 0.88 Li/TiO_2 i.e. to almost fully lithiation of the nanotubes. Whereas region (2) with an average lithium surface density of about $\lambda_2 \approx 15\ \frac{\mu g}{cm^2}$, corresponding to 0.53 Li/TiO_2, may represent an area where the nanotubes only undergo the first phase transition in the lithiation process [20]. For more details about galvanostatic lithiation/delithiation curves also see [8]. The origin of the so called hot spots and possible reasons for the presence of some electrode areas where the nanotubes only undergo the first phase transition are currently under discussion.

[8] Institute of Physical Chemistry, Universität Innsbruck.

5.3.4 Lithium Depth Profile in 4 μm long TiO_{2-x}-C Nanotubes

Another interesting question is how the lithium propagates into the nanotubes. Hence a depth profile of the lithium intercalation along the tubes would be very interesting to investigate the electrochemical processes going on there.
In this section the measurement of a sample (Sample 12, see Table B.1) characterized by TiO_{2-x}-C nanotubes with a length of about 4 μm, electrochemically lithiated, is presented. The sample was measured inside the mini-container, with a flux of cold neutrons of about $\Phi = 4.59 \cdot 10^8 \ \frac{\mathrm{n}}{\mathrm{cm^2 s}}$ over a runtime of about 900 s.
Fig. 5.15(a) shows the impact energy of tritium particles versus their impact angular coordinate φ on the detector plane. Tritium particles with energies within a range of about 2350 keV – 2650 keV are detected (see red lines in Fig. 5.15(a)), meaning that tritons do not only come from the electrode surface but also from a few μm deep and lose part of their energy passing through sample layers of titanium dioxide. The energy loss ΔE of tritons is strongly related to the mass layer ΔM which these particles have passed before reaching the detector.
Fig. 5.15(c) shows a projection on the Y axis of the histogram in Fig. 5.15(a) for $100° < \varphi < 118°$; the figure shows a rather homogeneous tritium energy distribution.
From the energy spectrum of Fig. 5.15(a) some information about the lithium depth profile in the sample can be extracted. The figure shows a constant lithium mass ratio $\frac{\mathrm{M_{Li}}}{\mathrm{M_{Ti}}} = \mathrm{const}$. This means that the lithium concentration per mass layer ΔM passed by tritium particles is homogeneous and does not depend on the spatial and geometrical arrangement of the nanotubes.
However the depth resolution of the measurement is limited by some factors, which are listed below:

- Multiple scattering in the 2 μm thick Mylar foil sealing the pinhole aperture. Tritium particles lose a small amout of energy (about 70 keV) passing through the Mylar window, which limits the energy resolution by the definition of the mass layer cut ΔM in Fig. 5.15(a). For comparison the same energy spectrum for a different sample with shorter nanotubes of 1 μm length (Sample 19, see Table B.1) - which was measured in "open-setup" without the presence of the Mylar window - is shown in Fig. 5.16. Here the lower energy edge of the ΔM cut is clearly identifiable with a rather good energy resolution given by the detector. The smearing of the upper energy edge is caused by pile up effects;

- High event rate during the measurement. This causes pile up effects and limits the energy resolution at high energies;

- Intrinsic energy resolution of the detector.

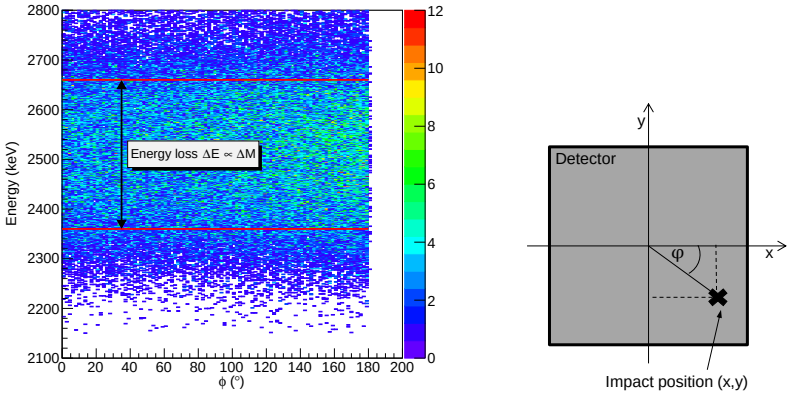

(a) (b)

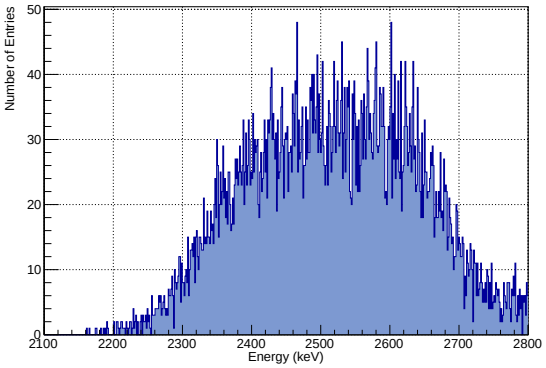

(c)

Figure 5.15: Data from the measurement of Sample 12 (4 μm long TiO_{2-x}-C nanotubes, electrochemically lithiated - see Table B.1).
(a) Impact energy of tritium particles versus impact angular coordinate φ on the detector plane. The red lines delimit the range of energies of tritons, whereas the white arrow defines the maximum energy loss ΔE corresponding to the electrode material layer ΔM of 4 μm long TiO_{2-x}-C nanotubes which tritium particles have passed before hitting the detector.
(b) Schematic representation of the detector plane; the angular coordinate φ is indicated.
(c) Projection on the Y axis of the histogram in (a) for $100° < \varphi < 118°$; the energy spectrum shows no significant structures.

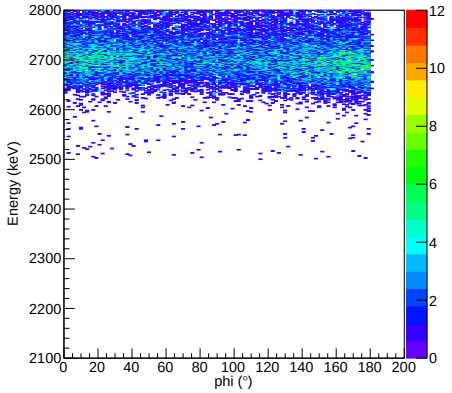

Figure 5.16: Impact energy of tritium particles versus impact angular coordinate φ on the detector plane from the measurement of Sample 19 (1 μm long TiO_{2-x}-C nanotubes, see Table B.1). The sample was measured in "open-setup". The spectrum shows a smeared upper edge due to pile up effects, whereas the lower energy edge is clearly identifiable.

Chapter 6

Lithium Measurements in Geological Samples

In the framework of this thesis the spatially resolved detection of tritium particles from the neutron capture reaction by lithium-6 was successfully applied to reconstruct the local lithium concentration in geological samples of so-called "pathfinder-minerals" containing lithium. The project was developed in collaboration with the Helmholtz Zentrum Dresden Rossendorf and the Helmholtz-Institut Freiberg für Ressourcentechnologie.
Two different sample typolgies were investigated. The first group consists of lithium-containing minerals extracted from lithium deposits, such as lepidolite from a pegmatite. A rather high lithium concentration in the percentage range is expected for these kind of samples. The second group consists of quartz minerals. Different quartz varieties such as agate, smoky quartz and red chalcedony were studied. A lithium content in the ppm range is expected for this quartz minerals.
Thin samples with a thickness below 1 mm were cut from the originl minerals. This was necessary in order to minimize the background from the massive ore material during the measurements. The aim was to fabricate samples as thin as possible, without demaging their mineral structure. Samples were fixed on pure aluminum target frames with a thickness of about 300 μm. Larger samples (with a diameter of about 25 mm) were fixed onto the upper and lower edge of the aluminum frame, whereas smaller ones were additionally fixed on a standard sample substrate covering the inner empty part of the aluminum frame.
Pinhole apertures were fabricated using a 100 μm thick Teflon[1] foil, stopping alpha and tritium particles, also fixed on identical target frames. Different hole diameters (about 2 mm and 0.4 mm) were fabricated, in order to achieve different spatial resolutions and efficiencies. Pinhole apertures were placed between target and detector at a distance of about 4 mm from the target, resulting in a magnification factor of about $\frac{b}{g} \approx 4$ (see Fig. 6.1). Therefore sample areas of about 5×5 mm^2 could be investigated using the 20×20 mm^2 active area of the PSD detector.
A reference target ($RT3$) with a well-known amount of natural lithium fluoride

[1] Teflon™

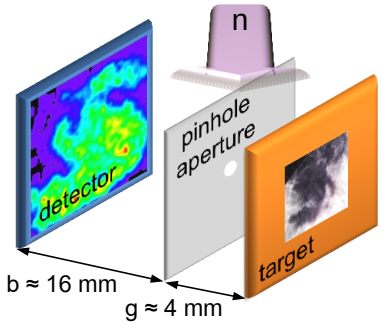

Figure 6.1: Measurement setup for lithium measurements in geological samples. Object distance g and image distance b are equal to about 10 mm, resulting in a magnification factor $\frac{b}{g} \approx 4$.

(about 3 $\frac{\mu g}{cm^2}$ ^{nat}LiF), homogeneously deposited on a standard target substrate by thin film deposition[2], was used to determine the absolute lithium content in the investigated minerals.
The reconstruction of the local lithium concentration in two of the studied samples, a quartz mineral and a pegmatite sample, is shown in this chapter to illustrate the method.

6.1 Lithium Measurement in a Quartz Sample

In this section the lithium content in an agate sample from Burgstall is studied (see Fig. 6.2).
Fig. 6.3 shows the energy spectrum from the measurement of the agate sample. First, the sample was measured without pinhole aperture with a neutron flux of about $\Phi_{n,th} = 2.72 \cdot 10^8 \frac{n}{cm^2 s}$ over a runtime of about $t = 1200$ s. The energy spectrum from a measurement run without pinhole aperture is shown in this context, since it shows a higher signal-to-background ratio and significantly different features due to the higher efficiency.
At low energies the spectrum is dominated by the background distribution (mainly γ and β particles), which decays exponentially on the right side and is cut by the trigger threshold of the data acquisition on the left side. At about $E = 1450$ keV the spectrum shows an additional gaussian distribution, which corresponds to alpha particles from the neutron absorption by boron-10. In the $^{10}B\,(n,\alpha)\,^{7}Li$ reaction [21] 94% of the outgoing ^{7}Li end up in its first excited state at 478 keV [2]. In this

[2]Target laboratory of the ZTL (Zentrales Technologie Labor), Department of Physics, Technische Universität München.

Figure 6.2: a: Photo of an agate sample from Burgstall.

case the alpha particle is emitted at an energy of 1473 keV while the lithium-7 is emitted at 841 keV. The peak like structure and its mean energy indicates that these alpha particles are emitted dominantly from the surface of the sample. A possible explanation would be a boron contamination on the sample surface, probably caused by the boron carbide used as cutting tool to fabricate the thin sample from the original mineral. At high energies the spectrum is dominated by tritium and alpha particles from the $^{6}\mathrm{Li}\,(\mathrm{n},\alpha)\,^{3}\mathrm{H}$ reaction. Tritium and alpha particles are emitted not only from the sample surface, but also from different material layers inside the sample, giving rise to homogenous count distributions over a specific energy range (see inset of Fig. 6.3). The tritium distribution starts at about 2700 keV and with a flat distribution goes down to small energies. For energies below 2055 keV the alpha and the tritium distributions overlap. Due to larger energy loss of alpha particles, their energy distribution is smeared out at even more. Therefore there is no clear step, but only a slight increase in the distribution below 2055 keV.
In order to reconstruct the lithum content in the sample only tritium particles with energies above $E_{t,min} = 2200$ keV are considered, since they can be clarly separated both from the background and from the alpha particles. From the energy loss of the tritium particles the studied sample depth is reconstructed with help of the well-known neutron depth profiling; quartz is used as stopping material. The investigated sample depth is equal to about $d_{SiO_2} = 2.5\ \frac{\mathrm{mg}}{\mathrm{cm}^2}$[3]. Dividing the lithium surface density by the effective sample thickness d_{SiO_2} the absolute lithium concentration in the sample is determined (see Sec. 4.2.2).
For the reconstruction of the local lithium concentration a measurement run with pinhole aperture was used. The sample was measured with a neutron flux of about $\Phi_{n,th} = 2.72 \cdot 10^{8}\ \frac{\mathrm{n}}{\mathrm{cm}^2\mathrm{s}}$ over a runtime of $t = 29551$ s. A sample area of about

[3]Calculated using SRIM - The Stopping and Range of Ions in Matter `http://www.srim.org/`

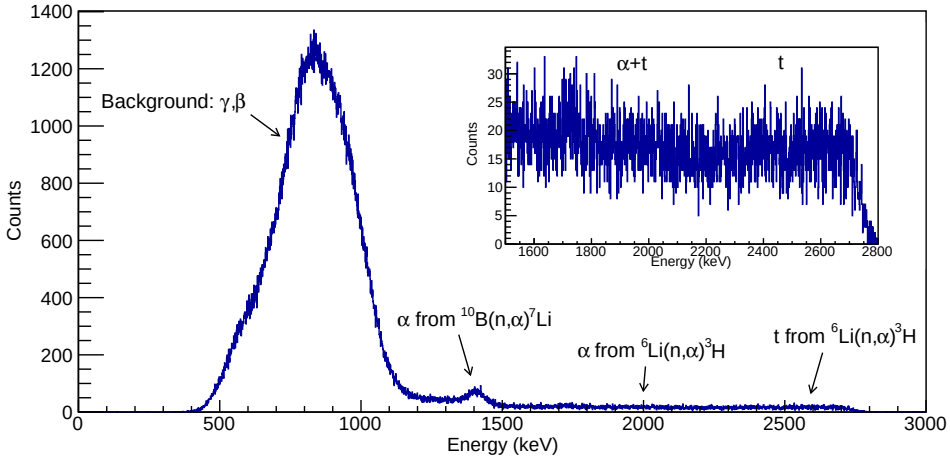

Figure 6.3: Energy spectrum from the measurement of an agate sample (see Fig. 6.4(c)).

5×5 mm^2 was investigated. Due to the low lithium concentration expected, the sample was measured with a pinhole aperture with a rather large size ($\varnothing \approx 2$ mm), providing a high efficiency and a still rather good spatial resolution of about 0.6 mm. The two-dimensional distribution of the absolute lithium concentration in the agate sample is shown in Fig. 6.4(a). A detailed description of how the local lithium concentration is reconstructed is shown in the next paragraph for a pegmatite sample (see chapter 6.2). Fig. 6.4(b) shows the local lithium concentrations after applying a gaussian blurring algorithm with a standard deviation of about $\sigma_{sf} = 0.35$ mm, in order to compensate statistical fluctuations. Region (1) shows a higher average lithium content of about $2.87 \pm 0.18 \pm 0.39$ ppm, whereas region (2) shows a lower lithium concentration below 1 ppm. Comparing the reconstructed distribution of the lithium concentration with a photo of the investigated sample area (see Fig. 6.4(c)), one can identify a correspondence between region (1) and the orange-coloured region on the left side of the picture, as well as between region (2) and the white-grey-coloured region on the right.

6.2 Lithium Measurement in a Pegmatite Sample

In this section the lithium content of a LCT pegmatite sample from Wodgina (Western Australia) is studied (see Fig. 6.8(c)).
The sample was measured with a neutron flux of about $\Phi_{n,th} = 1.00 \cdot 10^9 \, \frac{\mathrm{n}}{\mathrm{cm^2 s}}$, over a runtime of about $t = 5764$ s. A sample area of about 5×5 mm^2 was meas-

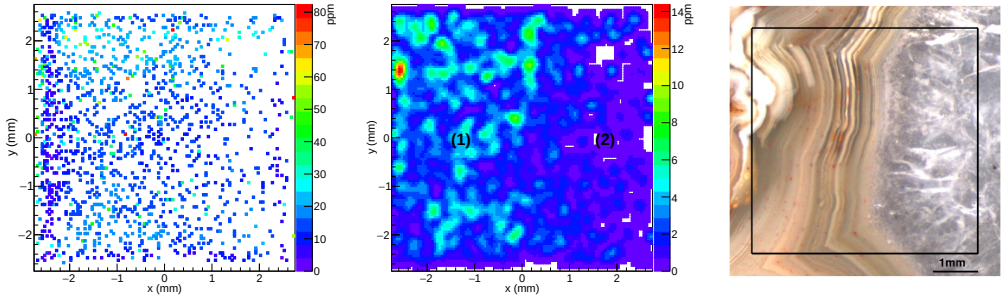

(a) (b) (c)

Figure 6.4: Lithium measurement in an agate sample.
(a) Two-dimensional distribution of the lithium concentration.
(b) Two-dimensional distribution of the lithium concentration after applying a gaussian blurring algorithm in order to compensate statistical fluctuations.
(c) Photo of the investigated sample area (black cut).

ured. The sample was measured with a pinhole aperture with a diameter of about 0.4 mm, providing a better spatial resolution but a lower efficiency. The effective spatial resolution of the measurement is dominated by the intrinsic detector resolution $\sigma_{det} = 300\ \mu$m.
Fig. 6.5 shows the energy spectrum from the measurement of the pegmatite sample (a zoom on the energy range $1100 - 3000$ keV is shown). In the inset of Fig. 6.5 a zoom on expected energies of alpha and tritium particles from the neutron absorption reaction by lithium-6 is shown. Again, only tritium particles with energies above $E = 2200$ keV are selected in order to reconstruct the lithum content in the sample, since they are clearly separated both from the background and from the alpha particles.
Fig. 6.6(a) shows the two-dimensional matrix $N_{t,ref}\,(x, y)$ of tritium particles with energies $E \geq 2200$ keV from the measurement of the pegmatite sample. Fig. 6.6(b) shows the same distribution for the reference target. The soft focus filter ($\sigma_{sf} = 80\ \mu$m) is applied to the reference position histogram, in order to compensate statistical fluctuations and avoid zero-counts bins. The reference target shows a homogeneous tritium distribution throughout the surface, as expected, except at the edges of the detector. Here an increased number of counts is observed; these do not have a physical meaning but are related to the detector readout pads. The reference target was measured with a neutron flux of about $\Phi_{n,th} = 2.72 \cdot 10^8\ \frac{\mathrm{n}}{\mathrm{cm^2 s}}$ over a runtime of $t = 10950$ s. Since the reference target was measured with a 2 mm diameter pinhole aperture, the corresponding tritium-ditribution histogram was scaled

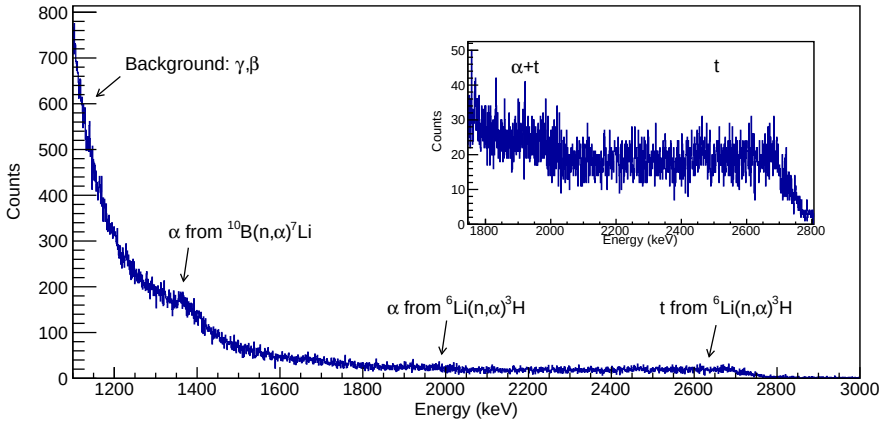

Figure 6.5: Energy spectrum from the measurement of a pegmatite sample.

with a solid angle factor $\frac{1}{25}$ from the ratio of the efficiencies by a 2 mm and a 0.4 mm aperture.
From the realtive measurement between sample and target the absolute lithium surface density $\lambda_{ref}(x,y)$ in $\frac{\mu g}{cm^2}$ in the pegmatite sample was reconstructed (see Fig. 6.7(a)). The lithium surface density is again divided by the effective sample thickness $d_{SiO_2} = 2.5\ \frac{mg}{cm^2}$ to get the absolute lithium concentration (see Fig. 6.7(b)). Fig. 6.8(a) shows the same histogram of Fig. 6.7(b) after applying a gaussian blurring algorithm ($\sigma_{sf} = 80\ \mu$m), in order to compensate statistical fluctuations. The sample shows an inhomogenous lithium concentration over the investigated area. It shows regions with a higher average lithium content of about $\langle c \rangle = 0.14 \pm 0.02\%$ (region (1) in Fig. 6.8(a)) and a region with almost no lithium content (below 0.006%, region (2)). Comparing the reconstructed concentration-distribution with a photo of the investigated area in the pegmatite sample (see Fig. 6.8(b)), it is evident that region (1) corresponds to the violet-coloured part in the middle of the picture, whereas region (2) corresponds to the white-coloured mineral.
From the energy loss of tritium particles the three-dimensional lithium profile in the pegmatite sample is reconstructed, which allows to investigate how lithium aggregations grow into the crystallites. The lithium depth profile for a selected sample region (see black cut in Fig. 6.9(a)) is shown in Fig. 6.9(b), where tritium counts with impact coordinate y in the range $0.5 - 1$ mm are plotett vs. impact coordinate x and emission depth z. $z = 0\ \frac{mg}{cm^2}$ corresponds to tritium particles emitted from the surface of the sample, whereas $z = 2.5\ \frac{mg}{cm^2}$ corresponds to tritium particles from the deepest sample layer accessible. For the specific selected region the lithium depth profile is not homogeneous throughout the investigated sample thickness. Some par-

ticular structures corresponding to different crystallites grown perpendicular to the sample surface can be distinguished. Again the resolution is limited by the rate of interactions in the detector material, indicated by a smooth edge in the energy spectrum shown in Fig. 6.5.

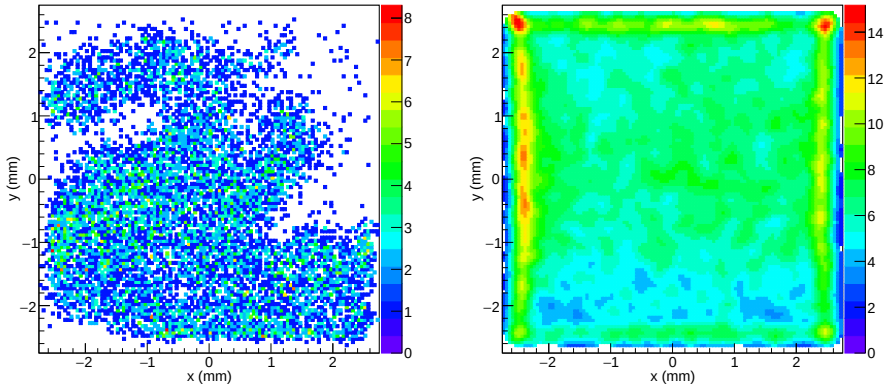

(a) (b)

Figure 6.6: Reconstructed emission points of tritium particles from the $^{6}\mathrm{Li}\,(\mathrm{n},\alpha)\,^{3}\mathrm{H}$ reaction in a pegmatite sample (a) and in the reference sample (b). Data for the reference sample have been smoothed by a blurring filter ($\sigma_{sf} = 80\ \mu\mathrm{m}$).

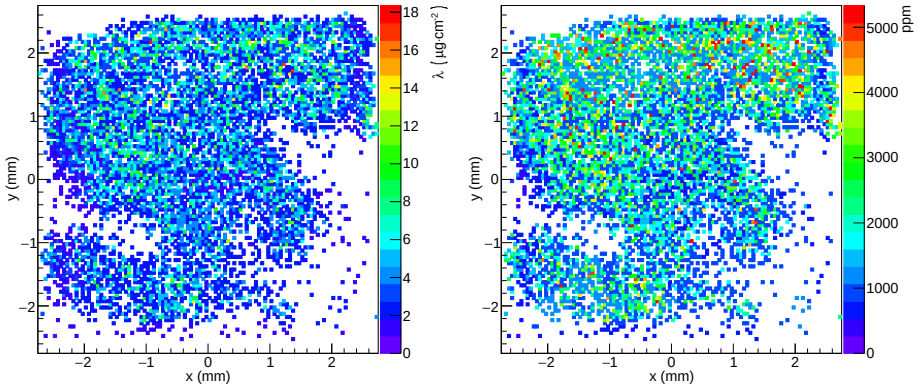

(a) (b)

Figure 6.7: Local lithium surface density (a) and local lithium concentration (b) for the pegmatite sample shown in Fig. 6.6(a).

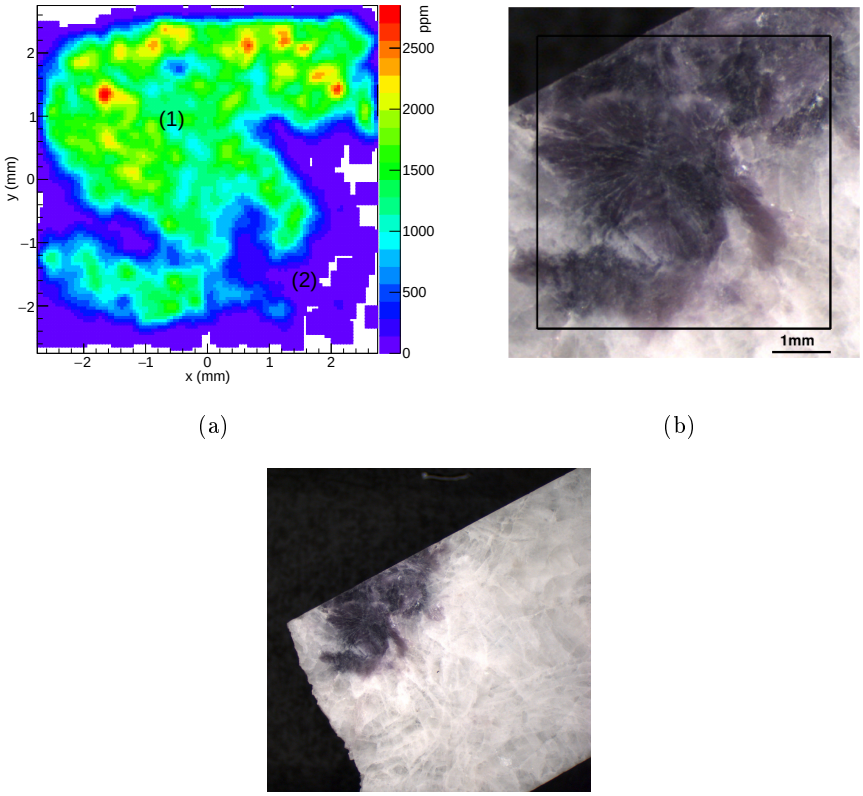

(a) (b)

(c)

Figure 6.8: a: Local lithium concentration of 6.7(b) after applying a gaussian blurring algorithm ($\sigma_{sf} = 80$ μm), in order to compensate statistical fluctuations.
b: Photo of the investigated sample region.
c: Photo of the pegmatite sample.

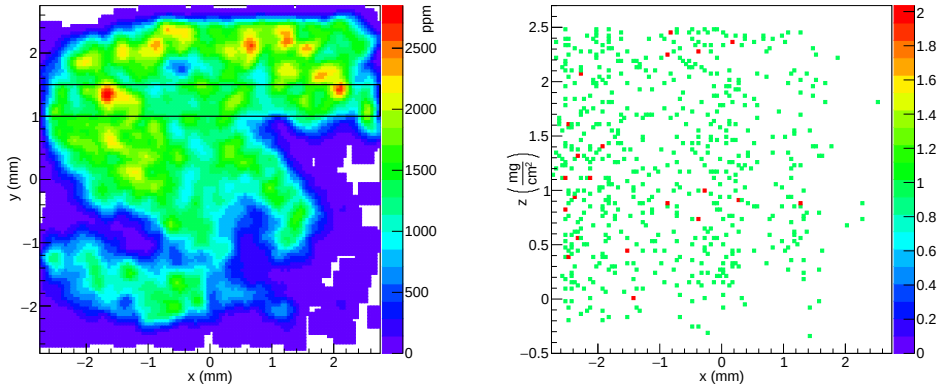

(a) (b)

Figure 6.9: Three-dimensional analysis of the lithium distribution in a pegmatite sample. Tritium counts with impact coordinate y in the range $0.5 - 1$ mm (black cut in (a)) are plotett vs. impact coordinate x and emission depth z.

Chapter 7

Conclusion and Outlook

One of the most peculiar properties of ^{6}Li is its extraordinary high neutron absorption cross section, which amounts to $\sigma_{n,th} = 940$ barn for thermal neutrons [2]. Based on this physical property of ^{6}Li, a special detector setup was developed in the framework of a DFG Project (GE 2296/1-1) and the PhD thesis of Josef Linchtinger [12], in order to detect lithium traces with cold neutrons. The method is based on the coincident detection of an alpha and a tritium particle from the neutron absorption reaction by lithium-6 and allows to detect extremely small amounts of this isotope, even down to the ppt range. The only limit consists in the sample thickness, which should be below d $< 1 \frac{\mathrm{mg}}{\mathrm{cm}^2}$ for composit material formed out of light nuclei.
In the framework of this Master's thesis the existing detector setup was modified, in order to study microscopic lithium distributions in thicker targets.
Samples were exposed to a flux of cold neutrons at the PGAA facility of the FRM II. Emitted charged particles were detected with a Position Sensitive silicon Detector (PSD). Information about the total lithium content were extrapolated from the total number of tritium particles hitting the detector. Special pinhole apertures were fabricated as imaging tool; they were introduced between target and detector, forming a sort of "camera obscura" which allowed to obtain a position resolution and reconstruct the three-dimensional profile of the lithium content in thicker targets. Different samples were analyzed.
First of all this experimental method was used to study one of the most promising materials for applications in lithium-ion batteries i.e. nanostructured titanium dioxide. This new precision method was succesfully applied to reconstruct the local lithium surface density in self-organized $TiO_{(2-x)}$-C and $Si/TiO_{(2-x)}$-C nanotubes - electrochemically grown on titanium substrate and charged with lithium ions - for the first time. Seventeen samples were investigated. Most of the samples showed a homogeneous lithium surface density over the whole electrode area, as expected, and an average lithium content comparable with results obtained by our collegues from the Innsbruck group, determined measuring the electrochemical charge upon lithiation. In some samples a larger electrode area was investigated; some of these samples surprisingly showed an inhomogeneous lithium surface density with regions

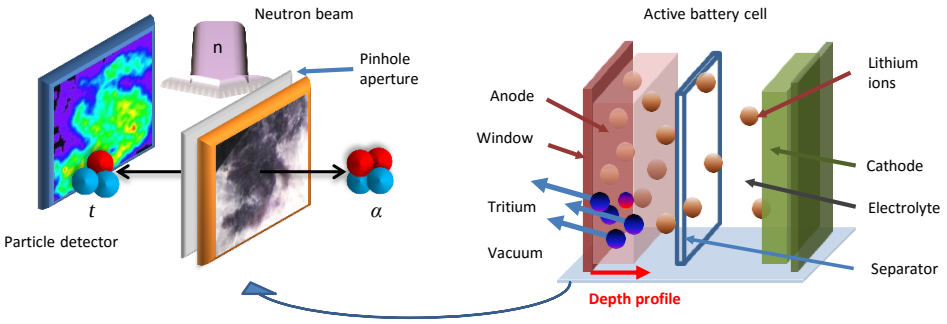

Figure 7.1: Four-dimensional isotope specific material depth profile with cold neutrons. Source: [22].

with even about 65% more lithium than other areas. Reasons for this inhomogeneities are currently investigated.
The position sensitive detection of tritium particles was additionally applied to reconstruct the three-dimensional lithium profile in geological samples, so called "pathfinder-minerals" containing lithium, like lepidolite $(K(Li,Al)_3(Si,Al)_4O_{10}(F,OH)_2)$ from a pegmatite. Twelve geological samples with different lithium contents from the ppm to the percentage range were studied. The position dependent lithium concentration was successfully reconstructed for all samples. From the energy loss of tritium particles the lithium depth profile was additionally studied.
In the framework of this Master's thesis two- and three-dimensional lithium measurements were performed. Future experiments with cold neutrons at the PGAA facility are already planned, with the purpose of performing four-dimensional lithium measurements i.e. additionally achieving a time resolution for dynamic processes during the intercalation of lithium in new electrode materials. The experimental setup will be similar to the one used in the framework of this Master's thesis, but it will be optimized to measure active targets such as active battery cells, in order to study how the intercalation of lithium ions in different electrode materials changes with time (see Fig. 7.1). Moreover the detector setup will be optimized to get even better spatial resolutions down to 100 μm in x and y.
Major limitations due to the background have to be overcome by using faster detectors with a higher segmentation. Also the intrinsic resolution could be drastically improved by segmented detectors with an ASIC based preamplification stage close to the sensors.

Appendix A

Design of Mini-Containers for TiO_2 Nanotubes Samples

In the following the design drawings of the fabricated mini-containers for the TiO_2 nanotubes samples are shown.

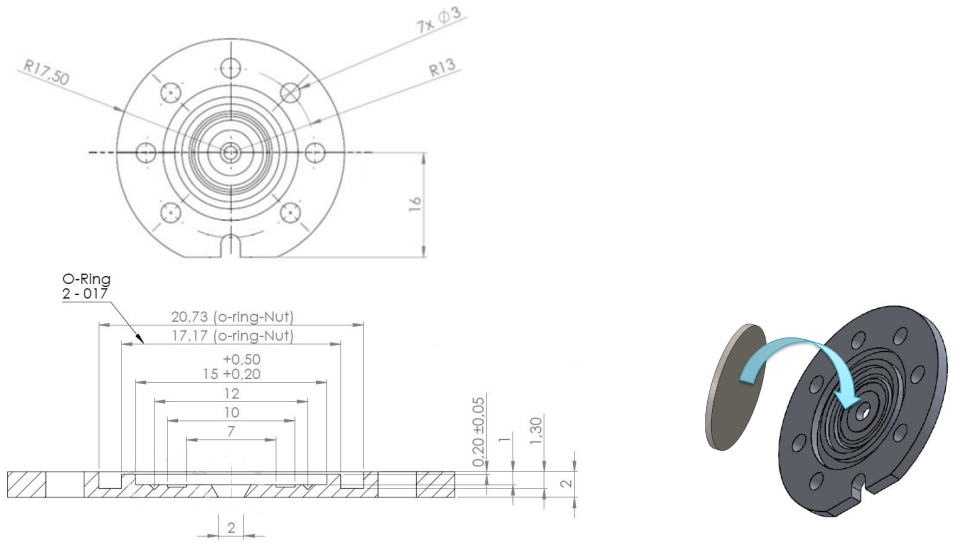

(a) (b)

Figure A.1: a: Design drawing of the front plate of the mini-container for the nanotubes samples with dimensions in millimeters.
b: Three-dimensional drawing of the front plate with a schematic representation of the titanium disk.

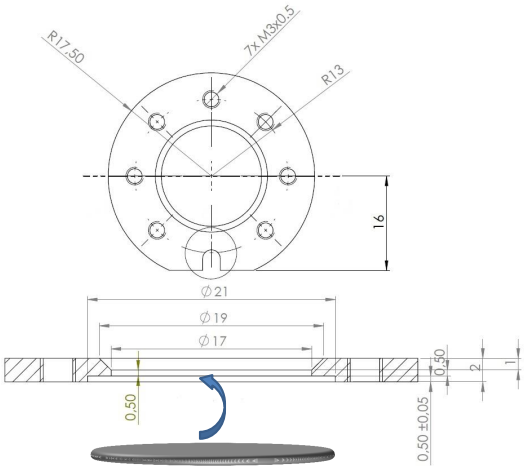

(a)

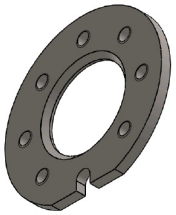

(b)

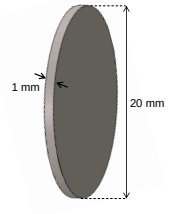

(c)

Figure A.2: a: Design drawing of the back plate of the mini-container for the nanotubes samples, with dimensions in millimeters and a schematic representation of the titanium disk.
b: Three-dimensional drawing of the back plate.
c: Three-dimensional drawing of the titanium disk.

Appendix B

TiO_2 Nanotubes - List of Results

Table B.1 shows a list of results obtained from the measurement of the TiO_2 nanotubes samples.

Sample Name	Sample Description	$\overline{\lambda}_{mini-cont}$ (μg cm^{-2})	$\overline{\lambda}_{open-setup}$ (μg cm^{-2})
Sample 2	TiO_{2-x}-C NT	$0.00 \pm 0.00 \pm 0.01$	
Sample 3	TiO_{2-x}-C NT, 1.1 V	$11.83 \pm 0.07 \pm 1.40$	
Sample 4	TiO_{2-x}-C NT, 0.04 V	$12.52 \pm 0.05 \pm 1.49$	
Sample 7	TiO_2 NT, 1.1 V	$14.18 \pm 0.07 \pm 1.68$	
Sample 10	Si/TiO_{2-x}-C NT, 1.1 V	$10.33 \pm 0.05 \pm 1.23$	$17.68 \pm 0.16 \pm 2.11$
Sample 12	TiO_2 NT, 1.1 V	$69.48 \pm 0.22 \pm 8.22$	
Sample 14	TiO_2 NT, 1.1 V	$4.33 \pm 0.03 \pm 0.52$	$6.93 \pm 0.07 \pm 0.84$
Sample 16	TiO_{2-x}-C NT, 0.04 V	$22.98 \pm 0.10 \pm 2.72$	$32.76 \pm 0.24 \pm 3.89$
Sample 17	TiO_2 NT, 0.04 V	$24.18 \pm 0.10 \pm 2.86$	
Sample 18	Si/TiO_{2-x}-C NT	$0.00 \pm 0.00 \pm 0.01$	
Sample 19	TiO_{2-x}-C NT, 1.1 V	$12.15 \pm 0.07 \pm 1.44$	$15.99 \pm 0.13 \pm 1.91$
Sample 20	Si/TiO_{2-x}-C NT, 1.1 V	$11.43 \pm 0.06 \pm 1.36$	
Sample 21	TiO_{2-x}-C NT, 1.1 V	$1.53 \pm 0.02 \pm 0.19$	
Sample 22	Si/TiO_{2-x}-C NT, 0.04 V	$23.66 \pm 0.10 \pm 2.80$	
Sample 24	TiO_2 NT, 1.1 V	$3.71 \pm 0.03 \pm 0.45$	$6.08 \pm 0.07 \pm 0.74$
Sample 25	Si/TiO_{2-x}-C NT, 0.04 V	$2.97 \pm 0.02 \pm 0.36$	
Sample 28	TiO_2 NT, 0.04 V	$5.87 \pm 0.04 \pm 0.70$	

Table B.1: List of results from the measurement of the TiO_2 nanotubes (NT) samples. Data from the measurements inside mini-container and in open-setup are shown. Sample description, lithiation potential, as well as average lithium surface density with statistical and systematic uncertainty are indicated.

Bibliography

[1] National Nuclear Data Center, Brookhaven National Laboratory. Chart of Nuclides, http://www.nndc.bnl.gov/chart/. Accessed: 2016-04-05.

[2] Database of Prompt Gamma Rays from Slow Neutron Capture for Elemental Analysis. International Atomic Energy Agency. Vienna, 2007.

[3] Noorden, Richard V.: A better battery. Chemists are reinventing rechargeable cells to drive down costs and boost capacity. In: *Nature* 507 (2014), March, S. 26–28. http://dx.doi.org/10.1038/507026a. – DOI 10.1038/507026a

[4] U.S. Geological Survey, 2015, Mineral commodity summaries 2015: U.S. Geological Survey, 196 p., http://dx.doi.org/10.3133/70140094. Accessed: 07-04-2016.

[5] U.S. Geological Survey, 2016, Mineral commodity summaries 2016: U.S. Geological Survey, 202 p., http://dx.doi.org/10.3133/70140094. Accessed: 07-04-2016.

[6] Hudson Institute of Mineralogy 1993-2016, http://www.mindat.org/, Accessed: May 2, 2016.

[7] Scrosati, Bruno ; Garche, Jürgen: Lithium batteries: Status, prospects and future. In: *Journal of Power Sources* 195 (2010), Nr. 9, 2419 - 2430. http://dx.doi.org/http://dx.doi.org/10.1016/j.jpowsour.2009.11.048. – DOI http://dx.doi.org/10.1016/j.jpowsour.2009.11.048. – ISSN 0378–7753

[8] Brumbarov, Jassen ; Kunze-Liebhäuser, Julia: Silicon on conductive self-organized TiO2 nanotubes - A high capacity anode material for Li-ion batteries. In: *Journal of Power Sources* 258 (2014), 129 - 133. http://dx.doi.org/http://dx.doi.org/10.1016/j.jpowsour.2014.02.049. – DOI http://dx.doi.org/10.1016/j.jpowsour.2014.02.049. – ISSN 0378–7753

[9] Kieffer, R. ; Jangg, G. ; Ettmayer, P.: *Sondermetalle: Metallurgie/Herstellung/Anwendung*. Springer-Verlag, 2013

[10] Ajzenberg-Selove, F.: Energy levels of light nuclei A = 5-10. In: *Nuclear Physics A* 490 (1988), Nr. 1, 1 - 225. http://dx.doi.org/10.1016/0375-9474(88)90124-8. – ISSN 0375–9474

[11] Tilley, D.R. ; Cheves, C.M. ; Godwin, J.L. ; Hale, G.M. ; Hofmann, H.M. ; Kelley, J.H. ; Sheu, C.G. ; Weller, H.R.: Energy levels of light nuclei A=5, 6, 7. In: *Nuclear Physics A* 708 (2002), Nr. 1-2, 3 - 163. http://dx.doi.org/10.1016/S0375-9474(02)00597-3. – ISSN 0375–9474

[12] Lichtinger, Dr. J.: *Quantitative Untersuchungen der lokalen Lithiumkonzentration im menschlichen Gehirn und ihr Bezug zu affektiven Störungen*, Technische Universität München, Physik Department E12, Diss., 2015

[13] Lichtinger, J. ; Gernhäuser, R. ; Bauer, A. ; Bendel, M. ; Canella, L. ; Graw, M. ; Krücken, R. ; Kudejova, P. ; Mützel, E. ; Ring, S. ; Seiler, D. ; Winkler, S. ; Zeitelhack, K. ; Schöpfer, J.: Position sensitive measurement of lithium traces in brain tissue with neutrons. In: *Medical Physics* 40 (2013). http://dx.doi.org/10.1118/1.4774053

[14] Ammon, W. von ; Blumenwitz, D. ; Böning, K. ; Didier, H.-J. ; Dubbers, D. ; Fischera, C.-O. ; Frey, F. ; Friedl, J. ; Gähler, R. ; Gerstenberg, H. ; Gläser, W. ; Gobrecht, K. ; Grift, J.F.J. van d. ; Gutsmiedl, E. ; Habs, D. ; Hassel, G. von ; Henkelmann, R. ; Ibel, K. ; Molls, M. ; Nuding, M. ; Peisl, J. ; Petry, W. ; Pfister, G. ; Roegler, H.-J. ; Rottmann, M. ; Schillinger, B. ; Schreckenbach, K. ; Springer, M. ; Steichele, E. ; Wagner, F. ; Waschkowski, W.: *Neue Forschungs-Neutronenquelle Garching*. Technische Universitt München, Projektgruppe FRM-II, 1997

[15] Révay, Zs. ; Kudějová, P. ; Kleszcz, K. ; Söllradl, S. ; Genreith, Christoph: In-beam activation analysis facility at MLZ, Garching. In: *Nuclear instruments & methods in physics research / A* 799 (2015), 114 - 123. 10.1016/j.nima.2015.07.063. – ISSN 0168–9002

[16] Experimental facilities Heinz Maier-Leibnitz Zentrum (MLZ). Forschungs-Neutronenquelle Heinz Maier-Leibnitz (FRM II), Technische Universität München, 2013. https://www.frm2.tum.de/fileadmin/w00bnv/www/Aktuelles___Medien/Broschueren/Sonstige/Experimental-facilities-MLZ-2013.pdf

[17] Canella, Lea ; Kudějová, Petra ; Schulze, Ralf ; Türler, Andreas ; Jolie, Jan: Characterisation and optimisation of the new Prompt Gamma-ray Activation Analysis (PGAA) facility at {FRM} {II}. In: *Nuclear Instruments and Methods in Physics Research Section A: Accelerators, Spectrometers, Detectors and Associated Equipment* 636 (2011), Nr. 1, 108 - 113. http://dx.doi.org/10.1016/j.nima.2011.01.126. – ISSN 0168–9002

[18] Brumbarov, J. ; Vivek, J. P. ; Leonardi, S. ; Valero-Vidal, C. ; Portenkirchner, E. ; Kunze-Liebhauser, J.: Oxygen deficient, carbon coated self-organized TiO2 nanotubes as anode material for Li-ion intercalation. In: *J. Mater. Chem. A* 3 (2015), 16469-16477. http://dx.doi.org/10.1039/C5TA03621F. – DOI 10.1039/C5TA03621F

[19] Obrovac, M. N. ; Christensen, Leif: Structural Changes in Silicon Anodes during Lithium Insertion/Extraction. In: *Electrochem. Solid-State Lett.* 7 (2004), S. A93–A96. http://dx.doi.org/doi:10.1149/1.1652421. – DOI doi: 10.1149/1.1652421

[20] Private communication Engelbert Portenkirchner, Institute of Physical Chemistry, University of Innsbruck.

[21] Göpfert, A ; Hambsch, F.-J ; Bax, H: A twin ionization chamber setup as detector for light charged particles with energies around 1 MeV applied to the ^{10}B(n,α)^{7}Li reaction. In: *Nuclear Instruments and Methods in Physics Research Section A: Accelerators, Spectrometers, Detectors and Associated Equipment* 441 (2000), Nr. 3, 438 - 451. http://dx.doi.org/10.1016/S0168-9002(99)00952-3. – ISSN 0168–9002

[22] BMBF application for Project 05H16W01

List of Figures

List of Tables

Acknowledgement

At this point I would like to thank all the people who supported me during the period of my Master's thesis.
First of all I would like to thank my supervisor, Prof. Shawn Bishop, for the interest and the attention showed for the project.
My warmest thanks also go to Roman Gernhäuser and Josef Lichtinger for the huge support that they gave me during all steps of my Master's thesis, in particular preparing the experiment and during the beam time in the reactor, as well as by the analysis. They always found some time for answering my questions and helping me in any problem coming up during the work. A big thank to Roman and Josef also for the great enthusiasm that they always showed working with me on this project.
Special thanks also to our collaboration partners in Innsbruck, in particular Prof. Julia Kunze-Liebhäuser and Engelbert Portenkirchner, as well as to Axel Renno and Georg Rugel from the Helmholtz Zentrum, for the great collaboration in the project.
Thanks also to the PGAA team, in particular Zsolt Revay and Petra Kudejova, for their support at the PGAA facility.
I would like to thank also Dominik Seiler, Sonja Winkler, Ralf Lang and Michael Klöckner for their help during the preparation of the experiment. Thanks also to Daniel Lubos for helping me with any kind of question about computer programming during the analysis.
I would like to thank also all members of the ex E12 group, who have warmly welcomed me into the group from the beginning. I really enjoyed the time working in the group and I'm glad to have met each of you.
My warmest thanks also go to Riccardo and to my family in Italy which were always with me, although the distance.
Again, my warmest thanks to all of you for contributing, in different ways, to make this time great.